

Spatial non-Destructive Imaging of Spin Domains in Bose-Einstein Condensates

Christian te Riet
3154246, University of Utrecht

August 29, 2014

Abstract

A simple experimental method is demonstrated to spatially and non-destructively image spin states in a BEC of sodium-23. The birefringent properties of the spin -1 and spin 0 states of the $F=1$ ground are used in combination with phase-contrast imaging to create a linear combination of two images taken in quick succession. We show that in the high detuning/low density limit the created linear combination is proportional to the density of either spin -1 or spin 0 states. The technique is used to estimate the spin drag coefficient of a spin -1 and spin 0 domains moving through in FORT under the influence of a spin dependent force.

Contents

i	THE TOPTICA TA-SHG PRO LASER SYSTEM	5
1	THE TOPTICA TA-SHG PRO LASER SYSTEM	6
1.1	The DL 100 Diode Laser	6
1.2	TA Pro Tapered Amplifier	8
1.3	The SHG Resonant Doubling Cavity	9
1.4	Past Issues with the TA-SHG System	12
ii	BEC EXPERIMENT LASER SETUP	14
2	FREQUENCY STABILISATION	15
2.1	Saturated Absorbption Spectroscopy	15
2.2	Frequency Modulation Spectroscopy	17
2.3	Saturated Absorbption Spectroscopy and Frequency Stabilization Setup	18
2.4	Laser Linewidth and Frequency Stability	21
3	EXPERIMENTAL SETUP	24
iii	NON DESTRUCTIVE SPATIAL IMAGING OF SPIN DOMAINS	27
4	EXPERIMENTAL SETUP	28
4.1	Creation of Bose-Einstein Condensates	28
4.2	PCI and Spin Dependent PCI Imaging	30
4.3	Rotating the Quantization Axis	35
4.4	Creating σ_+ and σ_- Polarized Light	36
5	NON DESTRUCTIVE SPATIAL IMAGING OF SPIN DOMAINS	40
5.1	Experimental Results of Spin Dependent PCI	40
5.2	Application: Spin Drag below T_c	43
5.3	Discussion	45
5.4	Conclusion and Outlook	50
iv	APPENDIX	53
A	THE LOCK-IN TECHNIQUE	54
B	POLARIZATION STATES AND TRANSITION STRENGTH	56
C	CABLE CONNECTIONS OF THE TA-SHG PRO	60
D	IMAGING SCRIPT EXAMPLES	62
	Acknowledgements	66

Part I

THE TOPTICA TA-SHG PRO LASER SYSTEM

The Toptica TA-SHG Pro Laser System

The Toptica TA-SHG Pro is a modular diode laser system assembled from several (nearly) individual components. Combined the system is able to deliver roughly 1.2 Watts of 589nm laser light with a linewidth below 500kHz, tunable over roughly 10nm. Here, a brief description of all laser components will be given for safe and quick operation.

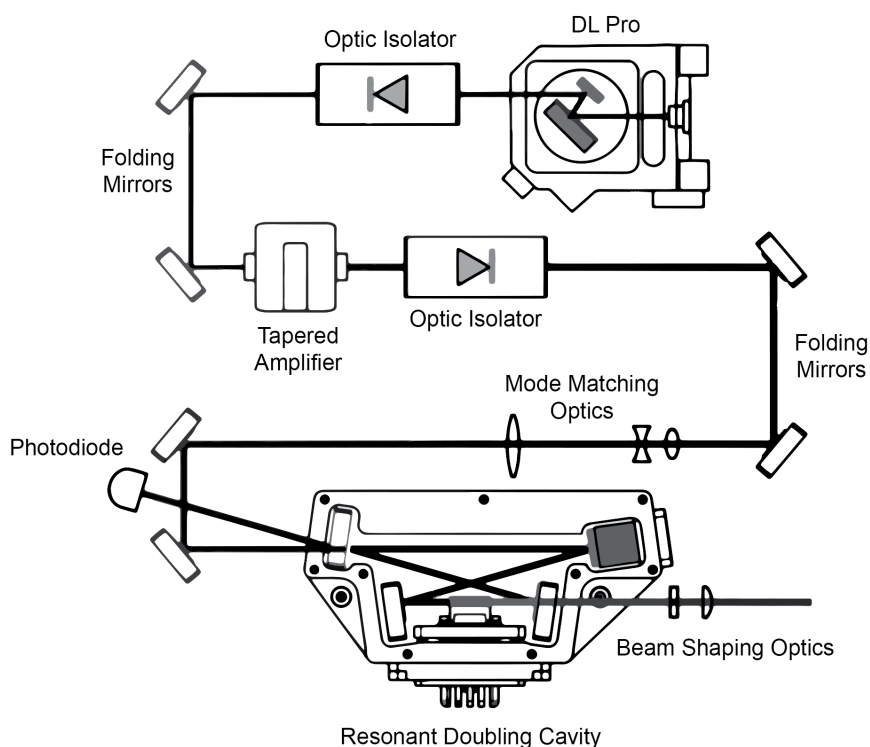


Figure 1.: Schematic layout of TA-SHG components. Light from the DL Pro is sent to the Tapered Amplifier and frequency doubled in the SHG cavity

1.1 THE DL 100 DIODE LASER

The most fundamental TA-SHG component is the Toptica DL 100 Pro high power laser diode. The DL100 contains an IR laser diode that delivers 80mW of 1178.40nm light at a set current of 346mA and has a bandwidth of about 1Mhz. This narrow bandwidth is achieved by collimating light emitted from the diode with a short focal length lens, letting it strike a reflection grating and back-reflecting the first reflection order into the laser resonator (a so-called Littrow setup). The rear facet of the diode and the grating together form an optical cavity. ¹ The free spectral range (FSR) of this cavity is substantially

¹ Toptica itself uses the terminology "an optical resonator that starts oscillating" and the complete DL100 is often referred by Toptica as "The Master Oscillator" for this reason

smaller than the FSR of the laser diode itself because the cavity length is of the order of a couple of centimeters, compared to only micrometers of the laser diode. This reduces the typical laser line width from some hundreds of Mhz to around 1 Mhz.

The diffraction grating offers another advantage. By changing the angle between emitted radiation from the laser diode and the grating itself, the wavelength of emitted the laser light can be adjusted. The DL100 wavelength can be adjusted in two ways:

1. Coarse: by manually adjusting the grating angle using the course grating adjustment screw
2. (Very) fine: by a combination of a piezo actuator controlling the grating angle and the current sent to the laser diode using a voltage

It is important to note however that the Littrow setup has a drawback: course adjustments to the grating angle will significantly affect the angle at which light is emitted from the laser cavity. When frequency adjustments are made, care should be taken to check if the emitted laser beam is still properly aligned with subsequent optical elements (specifically the TA).

To ensure that the laser diode has a large mode-hop-free region of operation and at the same time a very coarse frequency stability, the temperature of the DL 100 can be adjusted through a temperature controller, the DTC 110. Adjusting the temperature of the DL 100 in turn changes its cavity length and therefor its emitted frequency. Finding the correct grating, current, and temperature setting corresponding to a desired wavelength is therefore an iterative process.

The DL100 can be frequency modulated up to several tens of Mhz using separate, simultaneous modulation frequencies in order to perform Pound-Drever-Hall (PDH) or Lock-In (LI) stabilization with an external cavity or vapor cell. In the standard setup of the TA-SHG Pro, the DL100 by default is frequency modulated by the PDD110 with a modulation frequency of 20Mhz and a modulation depth of less than 100kHz to generate an error signal to stabilize the cavity length of the resonant doubling cavity.

Wavelength Adjustment

To adjust the wavelength, remove the top cover of TA-SHG 14074 to reach the course adjustment screw or insert a screwdriver into the side of TA-SHG 14095. Wear a grounding wrist strap before touching any electrical components inside the laser housing to avoid static electricity damaging (even destroying!) the laser diode. By carefully turning the screw one half turn clockwise/anti-clockwise, the laser wavelength can be respectively changed up or down approximately 5 nm from the center wavelength of 589nm.

When adjusting the wavelength mode hops will occur, discontinuously shifting the laser wavelength up or down by several tenths of a nanometer. Therefore, let a sample beam fall on a wave meter to determine the current wavelength. ²

After turning the course adjustment screw, the laser might no longer be operating in a single mode. Usually this is immediately apparent, as the laser intensity flickers and/or has significantly lower power than in regular operation. When in doubt, check

² Our lab has a Burleigh Wavemeter available for this purpose. For a standard frequency adjustment, 589.157nm is chosen as the center wavelength. Anything closer than $\pm 0.010\text{nm}$ is also acceptable as final adjustments can be made using the Digilock.

if the mode structure of the SHG doubling cavity is a series of evenly spaced sharp high peaks. If the laser is no longer in a single mode, adjust the diode current until it is. Now, check the wavelength. Repeat the procedure until the desired wavelength has been reached.

If the laser frequency is close to the desired frequency ($\pm \sim 0.010$ nm), it is more convenient to adjust the laser frequency by using an offset voltage in the Digilock controlling software, which by use of the Scan Control (SC100) controls both to the piezo actuator controlling the Litrow grating and the current sent to laser diode.

If the right wavelength cannot be reached due to mode hops, or if the laser is not operating in a single mode plateau around the desired wavelength (for instance, while scanning), increase (or decrease) the diode temperature by several degrees Kelvin and retry adjusting the wavelength.

Once the desired wavelength has been reached, measure the output power of the TA-SHG system. Adjusting the Litrow grating will slightly alter the beam emission angle, thereby affecting incoupling at the TA and possible the SHG resonant doubling cavity. If the power is significantly lower than the standard value (see the Toptica specs sheets) for the system, measure the power after the TA (see instructions in section 1.2). Perform a beam walk using the two TA incoupling mirrors until optimal IR power has been reached. Be very careful that at least some light seeds the TA, as an unseeded TA can generate damaging feedback oscillations. After the TA has been aligned, perform a beamwalk with the two SHG Resonant Doubling Cavity mirrors until optimal 589nm power has been reached.

Note: at all times prevent optical feedback into the DL100, as this could seriously damage or destroy the diode. Don't place objects into the laser beam emitted from the DL100 before the optic isolator.

1.2 TA PRO TAPERED AMPLIFIER

Single mode high power laser diodes are limited to optical powers of about 300mW. Therefore, amplifiers are needed to produce the high power needed in many research applications. The Toptica Tapered Amplifier (TA) is designed to offer a broad gain region of about 20nm while not deteriorating laser line width, frequency, or beam characteristics. Light emitted by the DL Pro is folded back by two mirrors and coupled into the TA (see figure 2). To ensure optimal coupling, a collimation lens is mounted in front of the entrance facet of the TA. TA's in general will produce elliptical beam profiles due to their tapered gain region. To compensate, a cylindrical lens is mounted on the back of the TA. The lenses are preadjusted upon delivery of the TA SHG Pro system and mounted with screws. Under normal operating conditions they shouldn't require any further adjustment. By performing a beam walk using the two mirrors, optimal coupling can be achieved. When operating the TA at a current of around 7 A, the TA will increase the total output power of the laser beam to around 2 Watts of 1178.4 nm (see the Toptica specs sheets).

Please note: NEVER switch on the TA without seeding it with laser light from the DL 100. An unseeded TA has a small chance to generate a feedback oscillations which can destroy the TA. By inserting the interlock plug into the back of the DC HP power supply, the TA and DL100 will automatically switch on together. Also, when performing main-

tenance on the DL 100, while the TA is switched off, prevent light from reaching the TA by blocking the beam.

Alignment

Unscrew the top cover of the TA-SHG housing. Flip up the TA reflection prism between the first two mirrors after the TA by inserting the appropriate hex key into the SHCS screw socket. Open the IR protection cover on the outside of the TA-SHG housing by pulling it upwards. If mirrors or optical elements are used, set up an appropriate beam dump for the IR beam. Place a power meter in the beam. Wear IR eye protection, as the emitted beam from the TA will surpass 2 Watts of IR light. Ensure that the cavity lock switch is set to 'Scan Mode'. This prevents the doubling cavity from attempting to find a locking point that is not there, and possibly damaging the piezo crystals in the SHG cavity. Switch on the TA-SHG system. Perform a beam walk using the two mirrors in front of the TA and optimize the IR power. IR power should reach 2.0 to 2.1 Watts. Once optimal power is achieved, turn off the system. Flip down the prism allowing light to reach the SHG cavity. Push down the IR protection cover.

1.3 THE SHG RESONANT DOUBLING CAVITY

The trapping and cooling of sodium requires light of 589nm. Currently, no laser diodes are available to produce narrow line widths at this wavelength. The TA-SHG system uses second harmonic generation to solve this problem.

To generate the required wavelength of 589nm used in the trapping and cooling of

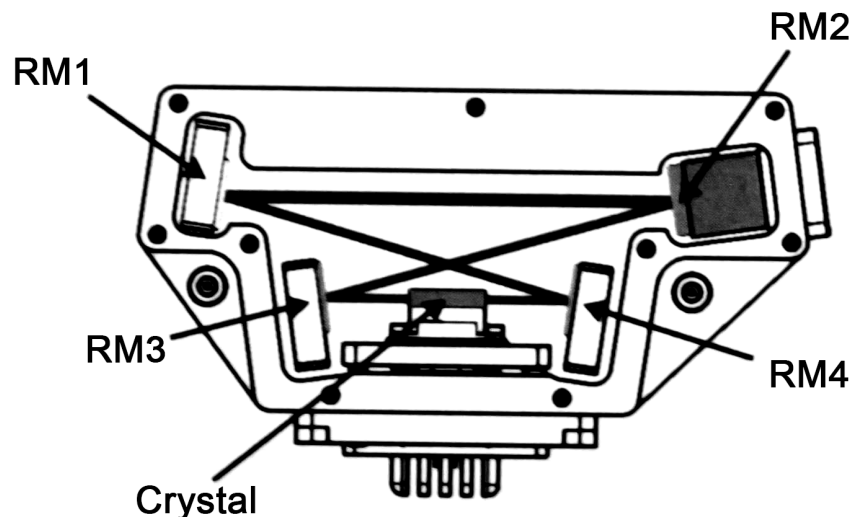


Figure 2.: Schematic layout the Resonant Doubling Cavity. Light from the TA is coupled into the SHG cavity by two mirrors. Piezo 1 and 2 behind Reflection Mirror 2 are controlled by the feedback loop based on the PDH technique keeping a constant cavity length.

sodium, the IR light leaving the TA needs to be frequency doubled. This is achieved by mode matching the high power IR beam leaving the TA and coupling it into a bow-tie

type resonant doubling cavity with a LBO crystal providing the second harmonic generation. Everything inside the SHG housing is preadjusted by Toptica and (because of the controlled environment) would most likely not require any further adjustments. To stabilize the index of refraction and phase matching properties, a temperature controller uses a thermoelectric cooler to stabilize the crystal temperature.

The doubling cavity length is stabilized by two stacked piezo crystals behind mirror 2. Light emitted by the laser diode is frequency modulated at 20 Mhz and a modulation depth of less than 100kHz by the Pound-Drever-Hall Detector (PDD) Module in the control rack. An internal photodiode monitors the intensity reflected back from the SHG cavity and an error signal is generated by the PDD through the Pound-Drever-Hall (PDH) technique. The error signal is used by two PID controllers, each controlling a single piezo, to stabilize the cavity length for optimal frequency conversion and linewidth control. One controller has a very narrow bandwidth but high recapture rate (the Fast Analog Linewidth Control/FALC), the other a large bandwidth with a slow recapture rate. The cavity length stabilization ensures the entire cavity acts as a frequency filter, reducing the linewidth to 500kHz. Before the laser light exits the TA-SHG Pro it passes a last collimating lens to ensure a near diffraction limited beam.

Please note: the crystal inside the SHG cavity is very sensitive to temperature changes and could possibly develop fractures if temperature changes too rapidly. When switching the connect DTC controller off, the TA-SHG system will automatically set the crystal temperature to 25 °C. When completely cutting off the TA-SHG system from power, make sure that the SHG crystal is first cooled to room temperature by adjusting the set point on the crystal DTC.

Alignment

By setting the laser to SCAN mode, a sawtooth voltage is applied to the piezo's thereby scanning the cavity length. When connecting the PD, PID OUT, and PID TRIG cables to an oscilloscope, the mode structure inside the cavity can be made visible. A selector switch on the PID110 allows the user to display the error signal generated by the PDD, and both the set level for locking and minimal intensity (MIN INTENS) for locking.

To properly align the SHG cavity, set the TA-SHG to SCAN mode with the dip switch on the Regulator PID front panel and connect the Mod Out channel to an oscilloscope trigger. Connect MON OUT to a scope channel. Connect the PD INT cable using the BNC T-connector to an oscilloscope channel ³. Perform a beam walk with the two the SHG cavity incoupling mirrors. Alignment is optimal when the mode structure looks like a series of sharp high peaks, where the high peaks are at least 10 times higher than the smaller peaks. Figure 3 shows a properly aligned cavity mode structure as well as an example of a misaligned cavity. Once alignment is complete, do not yet try to lock the SHG cavity.

³ The PD Int needs to stay connected to the PDD because otherwise the error signal cannot be generated and the laser system will be unable to lock

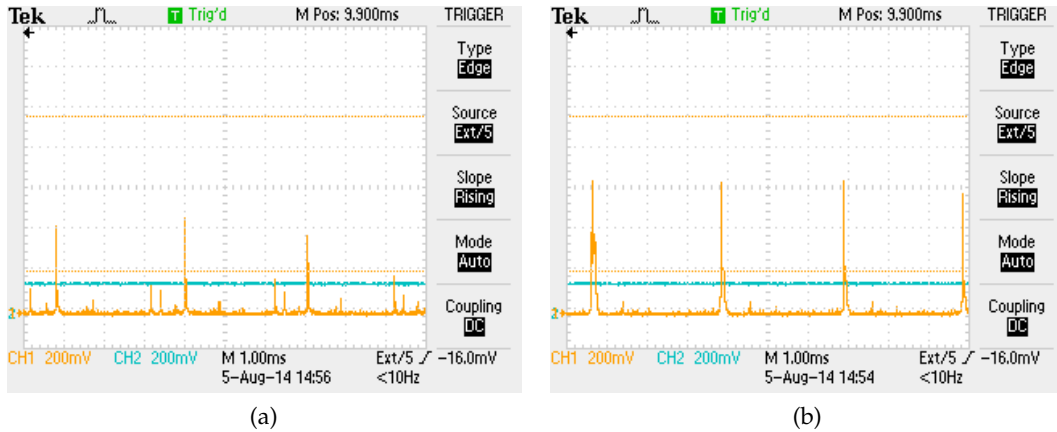


Figure 3.: (a) Mode structure of a misaligned SHG resonant doubling cavity. Notice the low intensity in the fundamental peaks and the non regularly spaced peaks (b) Mode structure of a properly aligned SHG resonant doubling cavity.

Locking the SHG Cavity

When the flip switch on the PID is set to LOCK, the FALC and PID controller attempt to stabilize the cavity length using the error signal generated by the PDD. For the locking mechanism to work, several parameters have to be set first. If the cavity lock has not been set or needs to be readjusted, perform the following steps.

Set the laser to SCAN mode and set the selector switch on the PID Regulator to MIN INTENS. Connect the PD Int and MON OUT connectors to an oscilloscope. Set the same zero level for both oscilloscope channels. Using a screwdriver, turn the MININTENS screw on the front panel so that it is well above small peaks in the mode structure, but below the high peaks. The cavity lock will now only be able to lock onto the high single mode peaks.

Next, set the selector switch to ERROR OUT. The error signal generated by the PDD will be shown. Using a screwdriver, turn the SET LEVEL screw until the ERROR OUT signal has zero offset.

Set the FALC Gain to zero. Reset the P, I, and D values on the regulator PID front panel using a screwdriver. Use intermediate settings for all gains and modulation amplitude (halfway through the full range of a knob) on the PDD and PID Regulator. Set the laser to LOCK on the PID Regulator front panel. The laser will attempt to lock, but fail. Increase the I part using a screwdriver until the system locks. Then increase P until the system starts oscillating, and then decrease P until the intensity oscillations disappear completely. Alternate between increasing I and P until oscillations appear, and turn back until the oscillations completely disappear.

To check if the SHG cavity PID settings are properly aligned, create a beat signal between system 14074 and 14095 using two overlapping beams on a single photodiode. Check if the Full Width Half Maximum of the resulting beat note is approximately 1MHz and that the beat has a approximately Lorentzian lineshape.

1.4 PAST ISSUES WITH THE TA-SHG SYSTEM

In the past, there have been several issues with the TA-SHG Pro system. Here, each issue will be briefly described for reference purposes.

Defective DC HP

Two issues have arisen with the DC-HP 7A power supply feeding the TA.

TA-SHG system 14074 was one of the first TA-SHG systems Toptica delivered with a DC-HP 7A power supply. During testing it was noted that a design error in the DC-HP created an oscillation at 57kHz in the supplied current over 5%, which directly resulted in 5% oscillations in the optical power of the amplified beam.

The oscillations were detected by letting (strongly) attenuated laser light from the SHG, TA and DL₁₀₀ fall onto a fast (VIS and IR sensitive respectively) photodiode connected to a spectrum analyzer. Light from the DL₁₀₀ was checked by using the out coupling port directly behind the first folding mirror on the exterior of the TA-SHG in 2. The source of the oscillations was determined to be from the TA. By using an alternate DCC/5A power supply, the oscillations disappeared.

The DC-HP was returned to Toptica and it was concluded a design flaw was the cause of the problem. All DC-HPs were redesigned internally, and a new version was delivered to our lab several months later.

The DC-HP for system 14095 short circuited during normal operation after 12 months and was no longer able to be switched off to standby mode. No indications of failure were noticed beforehand. When the DC-HP was switched on, but the TA-SHG system was switched off, the TA Current indicator light on the back of the TA-SHG indicated it was receiving current from the DC-HP, even though the DC-HP output itself indicated 0A. The problem was resolved by replacing the broken DC-HP with a new one. To our knowledge no damage was done to the TA itself.

Broken piezo in SHG cavity and PID controller

Either a short circuit in the PID controller of TA-SHG 14074 caused a broken piezo in the SHG cavity, or the broken piezo in the SHG cavity caused by a broken piezo.

The range of motion of the piezos inside the cavity became very limited. Locking the laser was extremely difficult, but was possible, and the lock would easily be broken again (by placing a post on the optical table, for instance). When scanning the cavity, only two single mode peaks were visible and a strong oscillation was present in the output of both the PID₁₁₀ and the DCC₁₁₀ (see figure 4). The combination of the PID₁₁₀ and the broken piezo was seen as the cause. Because the oscillations also reached the DL₁₀₀ (through the DC₁₁₀) the system was not switched on until the problem was resolved. The problem was solved by Toptica by installing a new PID₁₁₀ and completely new SHG cavity. To our knowledge, no damage was done to the DL₁₀₀ of system 14074.

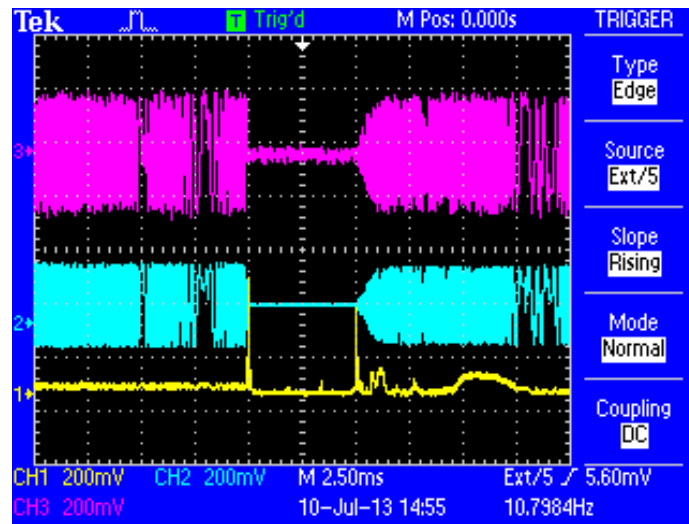


Figure 4.: Cavity scan using broken piezo and PID controller. CH1 is the PID INT, CH2 is the MON OUT of the PID₁₁₀, and CH3 is the MON OUT of the DCC₁₁₀

Part II

BEC EXPERIMENT LASER SETUP

Frequency Stabilisation

The output frequency of a diode laser typically depends on both the electric current through the diode and the diode temperature. When a laser diode is not locked to a reference (e.g. a cavity mode or atomic hyperfine transition) current and temperature fluctuations can over time (minutes to hours) cause the laser frequency to drift several hundreds of MHz from its starting frequency. In all our experiment, we wish to cool, trap and probe sodium using very specific atomic transitions. The four excited states of the sodium D2 line are respectively spaced 16, 34 and 58 Mhz apart, while the natural linewidth of sodium is roughly 10 Mhz. To successfully perform experiments using sodium it is therefore necessary for the laser frequency stability to be (much) less than the natural linewidth. To achieve this, we want to lock the laser frequency to an atomic hyperfine transition and ensuring that laser light itself has a narrow linewidth, by making use of two techniques: Saturated (or Doppler free) Absorbtion Spectroscopy and Frequency Modulation Spectroscopy (sometimes also Lock-In Modulation Spectroscopy).

2.1 SATURATED ABSORBTION SPECTROSCOPY

When the frequency of a laser beam passing through an atomic vapor is close to an allowed atomic transition, laser light can be absorbed. Due to the thermal motion of the atoms inside the vapour, atoms will see the laser frequency Doppler shifted depending on their velocity. The frequency range at which absorbtion of light passing through a vapor cell takes place is therefore Doppler broadened by several gigahertz obscuring the direct observation of the atomic hyperfine structure of all atomic transitions.

Saturated absorbtion spectroscopy [3] is a technique to identify the hyperfine structure of an atomic species. In saturated absorbtion spectroscopy, two overlapped and counter propagating laser beams of the same frequency are passed through a vapor of an atomic species of interest. One beam, the so-called pump beam, has a relative high intensity $I > I_s$ where I_s is the saturation intensity. The other beam, the probe beam, has a low intensity with $I \ll I_s$. The laser frequency is then scanned and the absorbtion of probe light by the vapor as a function of the frequency is measured with a photodiode.

For a beam of frequency f , passing probing an atom with an atomic hyperfine transition of frequency f_0 , the frequency dependent absorbtion coefficient takes the form of

$$\kappa = \frac{hf n_0 \alpha_0}{1 + 2I/I_{\text{textsat}}} \mathcal{L}'(f, f_0) \quad (1)$$

Here n_0 is the vapor density, α_0 the transition rate proportionality constant, and \mathcal{L} is a Lorentzian

$$\mathcal{L}'(f, f_0) = \frac{1}{1 + 4(f - f_0)^2 / \Gamma'^2} \quad (2)$$

Where the natural linewidth Γ is broadened due to the so called power broadening:

$$\Gamma' = \Gamma \sqrt{1 + 2I/I_{\text{sat}}} \quad (3)$$

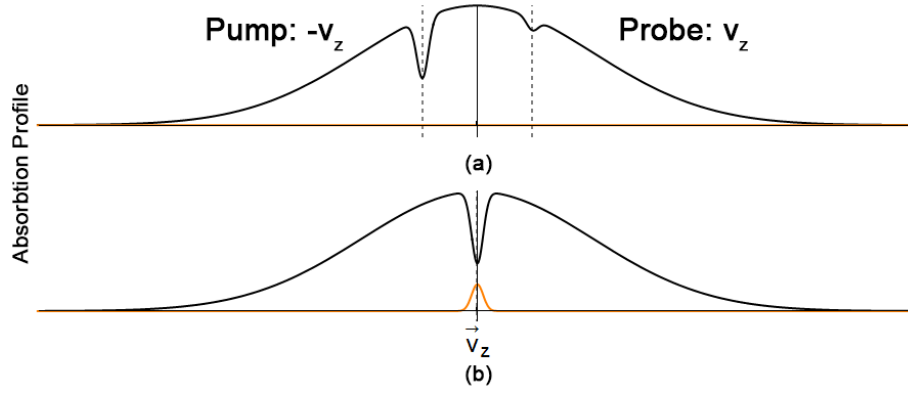


Figure 5.: Velocity dependent absorption profile of a single transition. (a) Pump (left) and probe (right) beam are respectively resonant with the transition frequency f_0 through two opposite velocity classes. (b) When both the pump and probe beam have a frequency such that both are resonant with f_0 through the velocity class $v_z = 0$, the probe beam will only be weakly absorbed by the vapor, because the strong pump beam has excited a significant part of the atomic population to an excited state. A sharp peak in transmission can then be detected using a photodiode.

A collection of atoms inside a vapor will experience a Doppler shift of the laser light according to their respective velocities along the propagation direction of the pump and probe beam.

$$f = f_0(1 \pm v_z/c) \quad (4)$$

Because the probe and pump beam counter propagate, this Doppler shift is opposite for the pump and probe beam. To find the total absorption coefficient for the vapor, we therefore need to average over all velocities. Assuming a Maxwell-Boltzmann distribution for the velocities of the atoms inside the gas, the total frequency dependent absorption coefficient becomes:

$$\kappa = \kappa_0 \exp(-(f - f_0)^2 / 2\sigma_v^2) \quad (5)$$

Where the width parameters σ_v is given by

$$\sigma_v = f_0 \sqrt{\frac{kT}{mc^2}} \quad (6)$$

And κ'_0

$$\kappa'_0 = \frac{\kappa_0}{\sqrt{1 + 2I/I_{\text{sat}}}} \quad (7)$$

With

$$\kappa_0 = n_0 h f \alpha_0 \sqrt{\frac{m}{2\pi kT}} \frac{c}{f_0} \frac{\pi \Gamma}{2} \quad (8)$$

Because the pump and probe beams counter propagate, the two beams will only be simultaneously resonant with atoms of the same velocity class when the probing frequency is such that it is resonant with atoms that have $v_z = 0$. In this case, the pump beam excites a significant fraction of the atoms with $v_z = 0$ to an excited state, thereby creating a dip in the velocity dependent absorption profile of the atomic transition. The probe beam then experiences a sharp drop in absorption which can be detected using a photodiode. Since probe and pump beam only address atoms with $v_z = 0$, the frequency dependent absorption becomes very sharply peaked Figure 5 illustrates this concept.

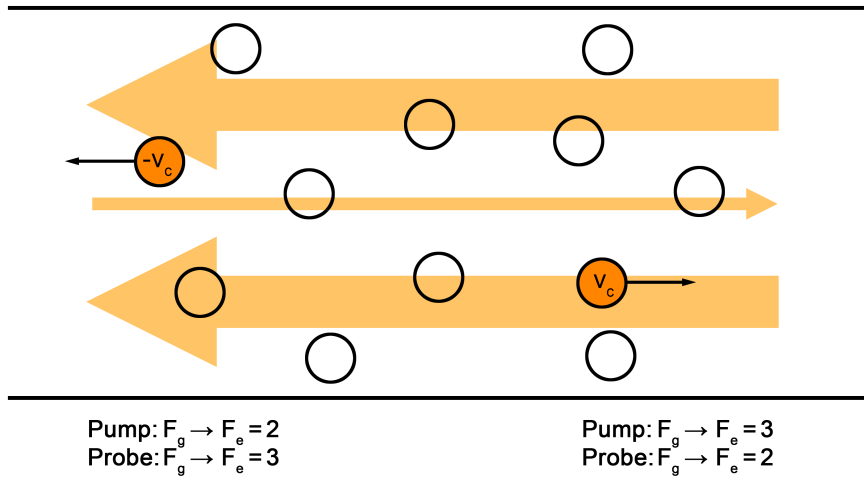


Figure 6.: Pump and probe beam respectively resonant with two different hyperfine transitions with two opposite velocity classes

In a systems with multiple excited and/or ground states, so-called crossover peaks will occur in a saturated absorption spectrum. Crossover absorption occurs when, due to the thermal motion of the atoms in the vapor and the resulting Doppler shift, the pump and probe beam are respectively resonant with two different atomic transitions each belonging to respectively two opposite velocity classes with $v_z \approx \pm c(f_2 - f_1)$ Figure 6 illustrates this concept. Because the absorption of the probe beam is significantly reduced, crossover absorption peaks occurs at a frequencies exactly in between any two allowed transition frequencies.

2.2 FREQUENCY MODULATION SPECTROSCOPY

In the BEC experiment, the main use of saturated absorption spectroscopy is to lock the laser frequency to a certain atomic transition. When the laser frequency drifts away from resonance, the probe beam light intensity detected by the photodiode decreases. Because of the symmetrical shape of the Lorentzian absorption profile, it is impossible to deduce if the laser frequency has increased or decreased using only an intensity measurement, and therefore impossible to create a feedback loop which drives the laser frequency back onto the resonance. A signal proportional to the derivative of the absorption signal could be used to solve this problem. It easy to show [1] [2] that by modulating the laser frequency with a modulation depth that is much smaller than the line width of the absorption line of interest and using a lock-in amplifier, just such a signal can be created (see appendix for a short explanation). This first derivative of the absorption signal is often called the error signal.

The derived error signal can then be used by a PID controller to stabilize the laser frequency.

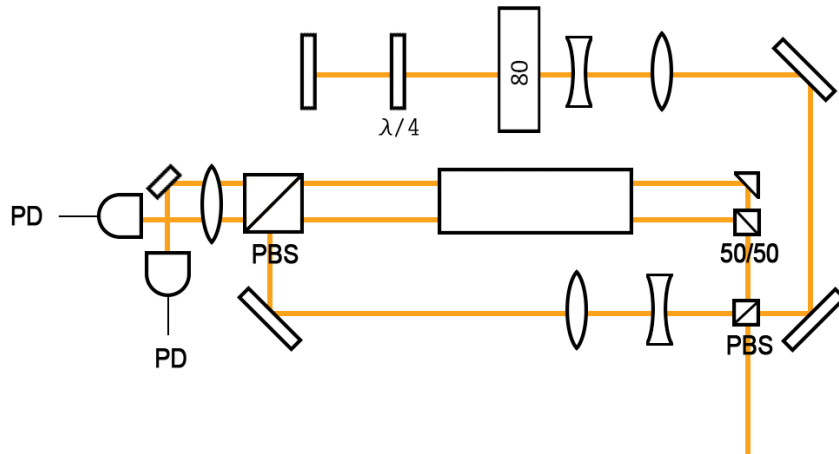


Figure 7.: Laser light is split in a low (probe) and high (pump) intensity part by a PBS. The pump is double passed through an AOM at 80Mhz and counter propagated onto the probe. Two probe beams of equal intensity are made using a 50/50 BS cube and a small mirror to create a flat Doppler free absorption spectrum

2.3 SATURATED ABSORPTION SPECTROSCOPY AND FREQUENCY STABILIZATION SETUP

The saturated absorption spectroscopy setup is as follows: Figure 7 shows the spectroscopy setup. Using a polarizing beam splitter cube and half wave plate, the beam is split into a probe and a pump beam part. Two parallel probe beams are created by passing the low intensity beam through a 50/50 beamsplitter cube and reflecting the remaining beam using a small mirror. One beam will be used as a probe beam, the other will serve as a reference beam to subtract absorption due to Doppler broadening from the saturated absorption spectroscopy signal. The mean intensity for each beam is $\ll 10\text{mW/cm} = I_s$. The two probe beams are passed through a cell filled with a sodium vapor held at a constant temperature of about 420K. Using two mirrors and another polarizing beam splitter, the pump beam is counter propagated onto one of the probe beams. Although the pump and probe beam now have perpendicular polarizations, changing the relative transition strength for each beam, the hyperfine structure is still easily identifiable from the saturated absorption spectroscopy signal. The pump beam is double passed through an AOM set to 80 MHz. Because the pump beam is double passed, pump and probe will differ 160 MHz in frequency. Due to this difference, note that pump and probe beam in this specific setup are simultaneously resonant only with those atoms in the velocity class that are Doppler shifted 80 MHz down with respect to the pump beam (or 80 MHz up with respect to the probe beam). The two probe beams are focused onto two photodiodes using a positive lens. The photodiodes themselves are connected to a Differential Amplifier (DA) which has a gain of $5 \cdot 10^6$ V/A and a bandwidth of about 100 MHz. The differential amplifier subtracts the reference beams from the probe beam to give a perfectly flat and Doppler free saturated absorption spectrum which is sent to the Digilock control software. Using the Toptica Digilock software and Digilock Controler module, the laser frequency is scanned with a rate of 5 Hz over a selected frequency range. The Digilock Controler module controls both the diode current and Littrow piezo by applying a triangular current to the laser diode and voltage to the piezo actuator controlling the Littrow grating, through the feed forward of the Scan Control. By varying the scan offset and amplitude voltage, the center scanning frequency

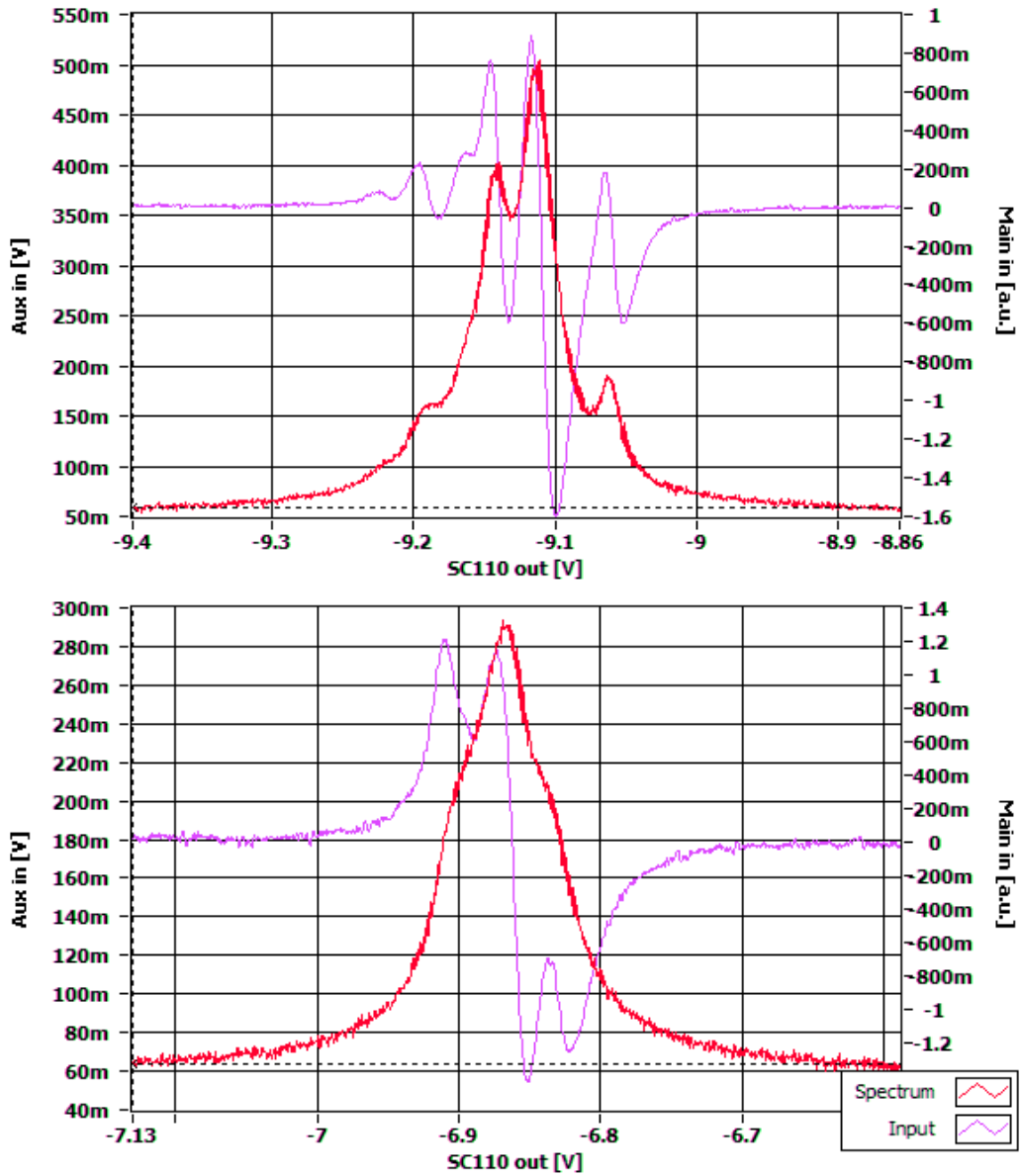


Figure 8.: Saturated absorption spectrum for $F_g = 2 \rightarrow F_e = 1, 2, 3$ (top) and $F_g = 1 \rightarrow F_e = 0, 1, 2$ (bottom) and generated error signal using the Digilock

can be chosen so that both $F = 1$ and $F = 2$ transitions are identifiable. The pump beam frequency is modulated with 80Khz and 0.400 V pp by using the internal Digilock oscillator, resulting in a modulation depth of the pump beam frequency of about 2 Mhz. The output from the DA is sent back to the Digilock where the signal is demodulated to generate an error signal. Figure 8 shows the $F_g = 1 \rightarrow F_e = 0, 1, 2$ and $F_g = 2 \rightarrow F_e = 1, 2, 3$ hyperfine transitions including crossover signals and the resulting error signal shape in the Digilock control software.

The error signal generated by the Digilock is used by two internal PID controller to stabilize the laser frequency. Like in the SHG cavity lock, both controllers are used simultaneously. PID controller 1 directly controls the laser current by sending a signal through 'Main Out' to the Mod DC connector of the DL100 and is used as a narrow bandwidth high recapture rate controller. Controller 2 controls the laser frequency through a backplane connection to the Scan Control module, which slightly adjusts both the laser current and the Litrow grating through use of the feedforward. Controller 2 is used as a (relative to PID₁) large bandwidth slow recapture rate controller.

Because the error signal generated by the Lock-In module has a high signal to noise ratio, and because frequency drift of the laser system due to temperature is a relatively slow process, the choice of the PID parameters is not very critical. The parameters found to be good to keep the laser in lock indefinitely and with good frequency stability are listed in table 1. If the laser lock becomes unstable or if the feedback signal becomes

	PID 1	PID 2
Gain	10	5
P	8000	15
I	10	7
D	0	0

Table 1.: PID Settings Digilock

prone to oscillations, the gain of the P part seem to be the most sensitive parameter. Decreasing P decreases the direct response of the error signal on a deviation from the set point, thereby making the system less likely to oscillate or become unstable. Decreasing P will of course also decrease the strength with which a deviation from the set point is corrected, but because temperature drift is such a slow process, the influence on the frequency stability is only limited.

It is useful (but not necessary) to enable the window comparator in the Digilock control software, in the 'Window' tab of the 'Autolock' module inside the Digilock control software. Using the window comparator, a maximum and minimum input signal voltage can be chosen to which the error signal will respond. If the error signal drifts outside of the window, no feedback is sent to the diode or Litrow grating and the laser is effectively operating in a free running mode. By using the window comparator, runaway feedback is prevented which otherwise could drive the laser frequency further and further away from the desired set point. Although runaway feedback is theoretically not damaging to the laser system, due to the fact that the DCC110 has a set current limit preventing any damage to the DL100, it could cause the laser system to jump to another single mode plateau with a slightly different center frequency. When this happens, it might be necessary to relocate the atomic hyperfine structure by changing the scan center offset.

Please note: Do NOT unplug any USB cables connecting a Digilock to a computer system while the Digilock software is running. Do NOT switch off the Digilock module before closing any Digilock control software or connections to a computer. Failure to do so, may:

- Reset all set values in the Digilock software.
- When two TA-SHG systems are connected to the Digilock control server simultaneously, cause the Digilock to connect to the wrong TA-SHG system
- When two TA-SHG systems are connected to the Digilock control server simultaneously, trigger a phenomenon preventing the Digilock software to connect to a TA-SHG system entirely

If any of these phenomena appear, close the Digilock software, switch off the Digilock module, and unplug all USB cables. Reconnect one USB cable. Switch on the Digilock module. Connect to the TA-SHG system. Properly close down the connection again. Connect the second USB cable and switch on the second Digilock module. Connect to the module. If this procedure fails, reconnect to both Digilock modules separately before connecting both modules to a computer using the USB cable.

2.4 LASER LINEWIDTH AND FREQUENCY STABILITY

To check the frequency stability of both the SHG Cavity lock (i.e. the laser linewidth) and the temperature drift stability, a beat signal was created between TA-SHG 14074 and 14095 using a photodiode with a bandwidth exceeding 2GHz (see figure 12 for setup). A major factor in the accuracy of the lock proved to be the alignment of the pump and probe beam and the derived error signal from the saturated absorption spectroscopy setup. This is illustrated in figures 10 and 9. Ideally, the setup is aligned in such a way that the error signal is symmetrically balanced around the $y = 0$ axis (the black 'balanced' signal), as can be seen in figure 9. When any adjustments are made to the spectroscopy setup, the error signal will start to look deformed and the locking point will shift in frequency several Mhz. Care should therefore be taken to realign the pump and probe beams such that the error signal looks like the 'balanced' signal in figure 9. As another test of the laser linewidth control and frequency stability, we locked the $F_g = 1 \rightarrow F_e = 1,2$ laser and scanned its frequency by changing the locking AOM frequency. By changing the AOM driving frequency by 1Mhz, the laser frequency is changed by 2Mhz (due to the double pass). We scanned of the $F_g = 1 \rightarrow F_e = 1$ and $F_g = 1 \rightarrow F_e = 0$ transition frequencies and used absorption imaging to measure the natural linewidth of sodium atoms trapped in the MT. The scan is shown in 11.

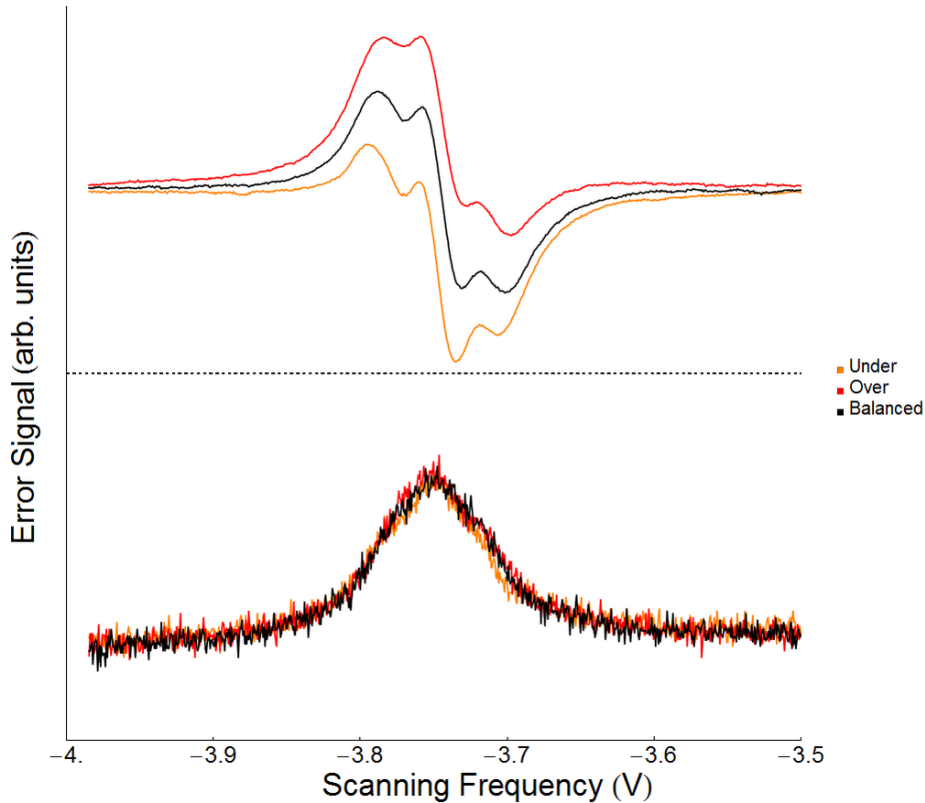


Figure 9.: 'Under', 'balanced', and 'over' tuned error signals derived from the saturated absorption spectroscopy setup by altering the overlap between pump and probe. The saturated absorption spectroscopy signal itself is not visible altered.

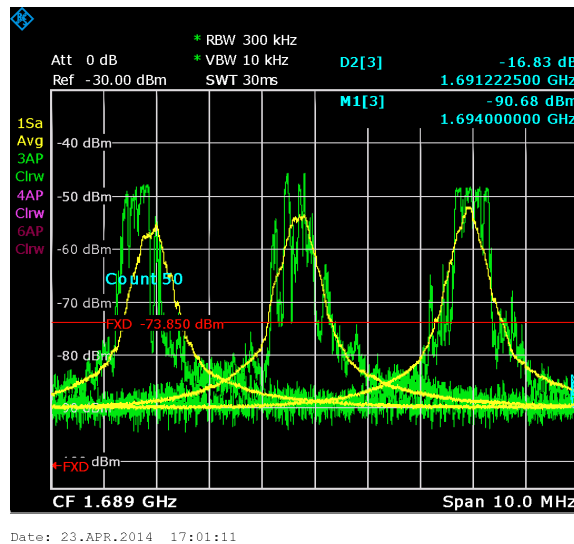


Figure 10.: Beat signal between between TA-SHG 14074 and TA-SHG 14095 locked to respectively the $F = 1 \rightarrow F = 1,2$ crossover and the $F = 2 \rightarrow F = 3$ transitions using a fast photodiode and a spectrum analyzer. From left to right, 'under', 'balanced', and 'over' tuned error signal. By changing the overlap between pump and probe beam, and keeping the same set point voltage for locking, the laser frequency can be shifted up or down by ~ 3 MHz. Note the FWHM of each beat note, which is less than 1MHz. We therefore conclude both TA-SHG systems to have linewidths or around 500kHz.

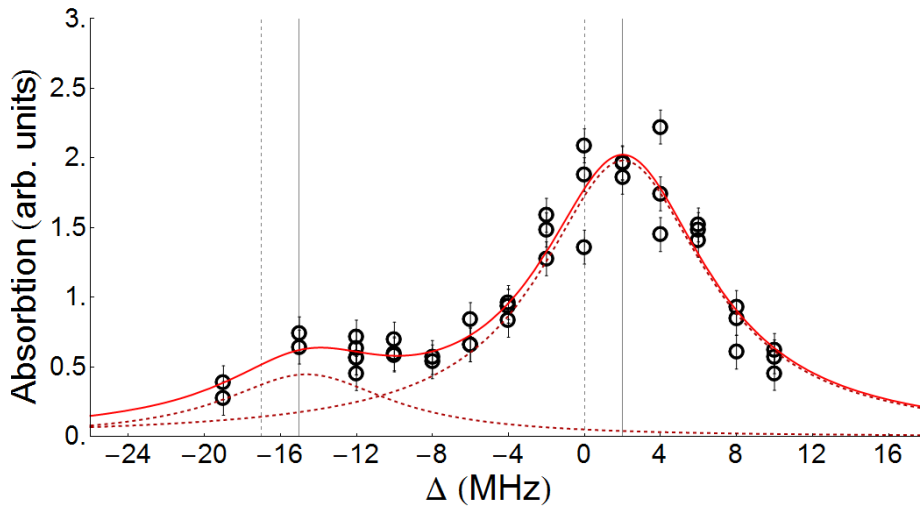


Figure 11.: Scan of the $F_g = 1 \rightarrow F_e = 1$ (right peak) and $F_g = 1 \rightarrow F_e = 0$ (left peak) transition frequencies using absorption imaging of atoms trapped in the MT at 300 ± 22 nK. The natural linewidth was determined to be 10.6 ± 0.6 MHz. This means that the laser linewidth itself must be smaller than this number and we can use laser light to trap and probe atoms on single atomic transitions. From the graph, we see a +2 MHz deviation from the frequency where absorption is expected to be maximum. This deviation is caused by a background magnetic field in the \hat{z} direction used as a quantization axis for the particles inside the MT during imaging, and the MT itself, which Zeeman shift the atomic transition frequencies.

Experimental Setup

Each beam used in the BEC experiment has its own branch on the optical table by using PBS cubes to split of an amount of power from the main beam. The PBS cubes are set up so that the low power beam leaves the cubes P polarized, as the extinction ratio of the PBS for P polarized light is $1/1000$ as opposed to $1/100$ for the S polarized light.

The waist diameter ($D_b = 2w = 4\sigma$) of the TA-SHG Pro lasers is $D_b = 2.6\text{mm}$. To ensure efficient coupling into fibers, all beams need to be able to pass AOMs without becoming clipped or distorted. We therefore use telescopes with a magnification factor of 0.333 to create a beam of $D_b = 0.87\text{mm}$ which can now easily pass even AOMs with a clear aperture of only 1mm. The Rayleigh range at this beam diameter is approximately 1 meter. We strive to have light arrive at a fiber incoupler after 40cm.

The fiber type we use is the Thorlabs 460-HP APC/PC with an NA of 0.12 and a Mode Field Diameter of $3.4\ \mu\text{m}$. To have efficient incoupling, the focused beam waist diameter therefore needs to be smaller than

$$D_f = \frac{4f\lambda}{\pi D_b} < 3.4\ \mu\text{m} \quad (9)$$

Here D_f is the waist diameter of a diffraction limited focussed beam of wavelength λ after passing a lens with focal distance f . Solving for f we find that a focal length of $f = 3.9\text{mm}$ would be required. No out-of-the-box fiber coupling solution exists with a focal length of 3.9mm. The nearest solution available was the Thorlabs Fiberport PAF-X-5A which has a focal length of 4.6mm. Of course, we could use another telescope after an AOM to increase the beam diameter, but this was deemed to give little extra efficiency. Testing the PAF-X-5A and the 0.87mm beam we arrived at an average incoupling efficiency of $\sim 70\%$, a vast increase over the very low fiber coupling efficiencies of about 30% in the old BEC Experiment setup. The different detunings of each branch and its power is listed in table 2. Figure 12 gives a schematic view of the entire light generation part of the BEC experiment setup.

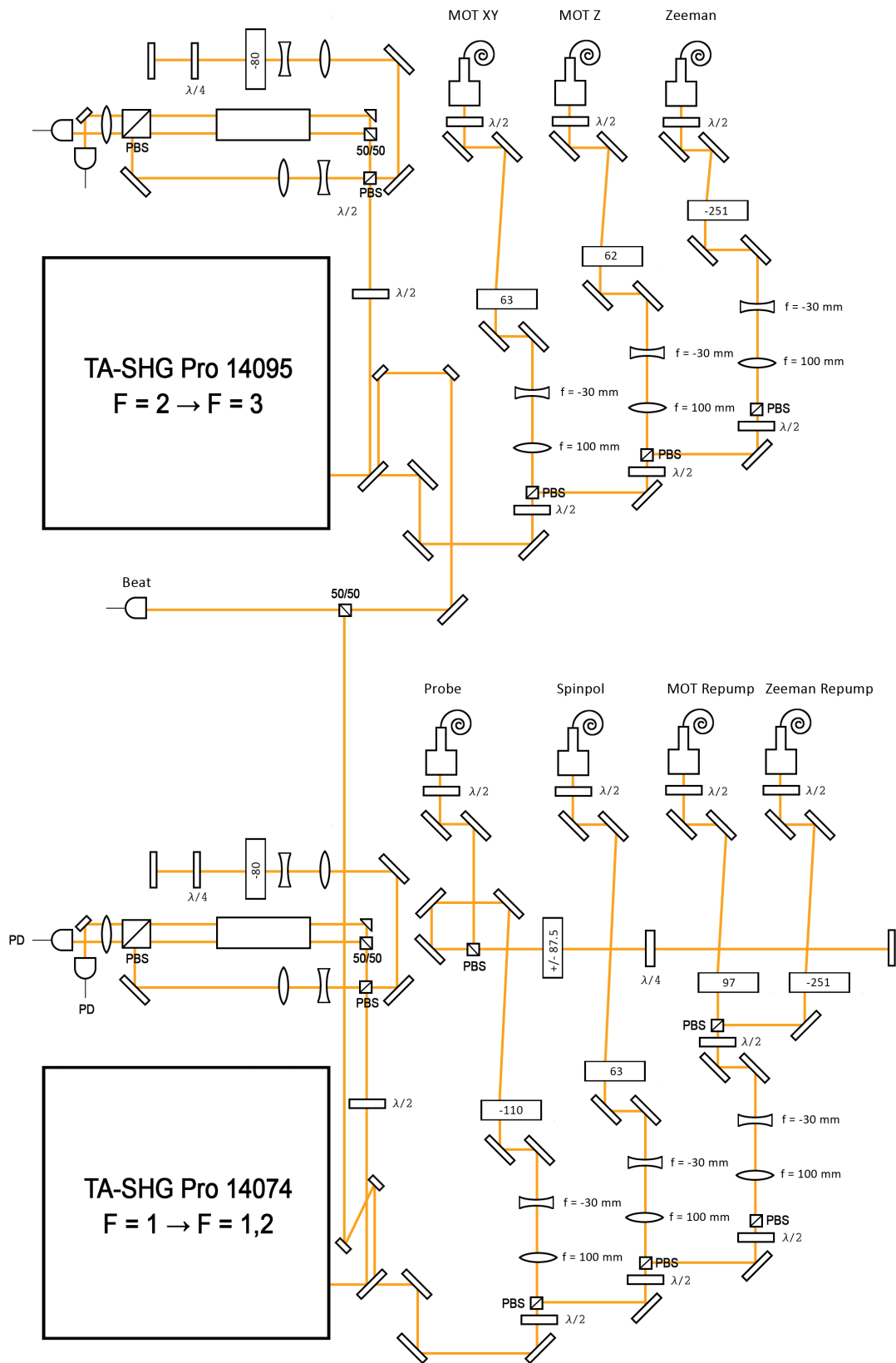


Figure 12.: Schematic overview of setup used to generate the different frequencies of light used in the BEC experiment

Beam	Power (mW)	AOM (Mhz)	Detuning	Transition
Repump (MOT)	30	97	0	$F_g = 1 \rightarrow F_e = 2$
Repump (Zeeman)	100	-251	-348	$F_g = 1 \rightarrow F_e = 2$
Probe (Base AOM)	10	-110	-	-
Probe	0.06	87.5×2	2*	$F_g = 1 \rightarrow F_e = 1$
Probe (PCI)	0.06	-87.5×2	-350	$F_g = 1 \rightarrow F_e = 1$
Zeeman Slower	~ 500	-251	-331	$F_g = 2 \rightarrow F_e = 3$
MOT Z	6	67	-13	$F_g = 2 \rightarrow F_e = 3$
MOT XY	24	66	-14	$F_g = 2 \rightarrow F_e = 3$

Table 2.: Power and frequency values for AOMs and beams in the BEC experiment setup.

*The 2MHz deviation from the $F_g = 1 \rightarrow F_e = 1$ transition was chosen so that the probing frequency in absorption imaging corresponds to the absorption maximum measured in figure 11.

Part III

NON DESTRUCTIVE SPATIAL IMAGING OF SPIN DOMAINS

Experimental Setup

4.1 CREATION OF BOSE-EINSTEIN CONDENSATES

All our experiments are based on the creation and manipulation of large Bose-Einstein Condensates (BEC) of Sodium-23 using laser and evaporative cooling. Here, a very short overview of the creation of BECs is presented to give some background to our experiment. For more detailed information of both the experimental techniques discussed or the experimental setup, see references [6], [7] or [8]

A beam of sodium atoms is created by heating blocks of sodium to ~ 600 K in an oven with an opening connected to a series of vacuum chambers. As hot atoms flow out through the opening and travel towards the main experimental chamber (the BEC chamber), several diaphragms inside the vacuum chambers ensure a collimated beam of atoms is created. Counter propagating to the beam of atoms are two overlapping, high intensity laser beams ¹ 251 Mhz red detuned to the sodium $3^2S_{1/2}F_g = 2 \rightarrow 3^2P_{3/2}F_e = 3$ (cooling) transition and $3^2S_{1/2}F_g = 1 \rightarrow 3^2P_{3/2}F_e = 2$ (repumping) transition. Through absorption, incoming photons transfer their momentum to the sodium atoms. Because the reemission of a photon through spontaneous decay occurs in a random direction, the repeated absorption and emission of light effectively exerts a net force on the sodium atoms in the direction of the Zeeman slower beam, slowing the incoming hot atoms.

There is a finite chance for atoms to be excited to the $F_e = 2$ state followed by decay to the $F_g = 1$ ground state, losing them from the cooling transition loop. The repumping beam is used to pump atoms from the $F_g = 1$ ground state back to the $F_e = 2$ state, where they will (eventually) decay to the $F_g = 2$ state to be cooled further.

To compensate for the decreased Doppler shift of the cooling light experienced by steadily slower moving atoms as they progress towards the BEC chamber, a magnetic field gradient created by a series of coil windings keeps the atoms resonant with the cooling and repumping transitions by using the Zeeman effect to shift the atomic resonance frequency. The entire cooling setup bears its name: the Zeeman slower.

When the atoms enter the Zeeman slower they have a velocity of about 700 m/s, the laser cooling inside the Zeemanslower reduces this to about ~ 60 m/s.

Atoms entering the BEC chamber are trapped in a Dark Spot Magneto-Optical Trap (MOT). The MOT consists of a quadrupole magnetic field and six counter propagating laser beams along three perpendicular axes which are slightly red detuned to the $F_g = 2 \rightarrow F_e = 3$ transition. The quadrupole field Zeeman shifts the atomic resonance frequency depending on atoms position inside the trap, increasing the likelihood an atom moving away from the center receives a kick back. To prevent loss of atoms to the $F_g = 1$ ground state, a repumping beam slightly detuned from the $F_g = 1 \rightarrow F_e = 2$ transition with a dark spot in the center keeps atoms from becoming lost from the cooling cycle. The dark spot allows for atoms in the center of the trap to reach their absolute ground

¹ Might not yet be the case. In the old setup an EOM was used to create a beam of radiation with frequency sidebands with more or less the same characteristics as described

state without being pumped to an excited state, raising their temperature and reducing their radiation pressure. Inside the MOT, atoms reach speeds up to several cm/s, or temperatures of several hundred micro Kelvin.

Because the MOT relies on the use of the absorption of laser light, there is still some energy being transferred into the system preventing the system to reach below critical temperatures allowing the formation of Bose-Einstein condensates. The primary limitation to laser cooling is the Doppler limit, where the Doppler shift is on the same order of magnitude as the natural linewidth of the atoms to be cooled. Once this temperature is reached, the cooling mechanism is no longer able to selectively address hot/high velocity atoms and the limits of this cooling mechanism are reached. To perform the final cooling steps, atoms are transferred from the MOT first into the Magnetic Trap (MT) and subsequently into the Far Off-Resonance Trap (FORT) to perform the final cooling steps.

To cool below the Doppler limit, a very strong magnetic field gradient is created to capture the already substantially cooled atoms from the MOT. After spin polarizing atoms to the $|F_g = 1, m_g = -1\rangle$ state, atoms are loaded into the so called Magnetic Trap (MT) and all resonant light is switched off. The MT consists of two field gradients, 118G/cm² radial and 42G/cm² axial, which create a central magnetic field minimum in the center of the trap. Due to the Zeeman effect, $|F_g = 1, m_g = -1\rangle$ particles are low field seekers and are therefore confined around the magnetic field minimum. $|F_g = 1, m_g = 0\rangle$ particles feel no force, and $|F_g = 1, m_g = +1\rangle$ are so called high field seekers and therefore expelled from the trap. By spin flipping high energetic particles by selectively applying RF pulses, high energetic particles are removed from the MT. This process of evaporative cooling can reduce the average temperature of the atoms to several hundred nano Kelvin (to even below T_c). For our present purpose, however, we will let atoms condense inside the FORT, where our main experiment takes place.

The FORT consists of a strongly focused beam of far detuned laser light to create a strong electromagnetic field gradient which exerts a force on electric dipoles, in this case the sodium atoms. The resulting trapping potential is given by [9]:

$$U(r, z) = -I(r, z) \frac{3\pi c^2}{2\omega_0^3} \left(\frac{\Gamma}{\omega - \omega_0} + \frac{\Gamma}{\omega + \omega_0} \right) \quad (10)$$

Here

$$I(r, z) = \frac{2P}{\pi\omega_0^2} \left(\frac{\omega_0}{w(z)} \right)^2 \exp \left(\frac{-2r^2}{w(z)^2} \right) \quad (11)$$

Where r is the radial distance from the FORT center, P the power of the used laser beam, ω_0 its angular frequency, and $w(z)$ the beam waist at a distance z away from the FORT focal point along the axis of the FORT.

To form a BEC, the sample is cooled using evaporative cooling. By reducing the power of the laser beam the well depth of the trapping potential is decreased. As the well depth decreases, the trap will only be able to hold atoms lower and lower kinetic energy. If the trap well depth is lowered slowly enough, only the top most energetic atoms ($\approx 10k_bT$ from the mean in the Maxwell-Boltzmann distribution) resulting from mostly two body collisions are removed, meaning kinetic energy is actively being removed from the system. Even though a 90% of the atoms might be lost from the trap, the extreme low temperature of several hundred nano-Kelvin can be reached needed to form Bose-Einstein Condensates.

In this thesis, we are specifically interested in the imaging of the two spin states $|F_g = 1, m_g = -1\rangle$ and $|F_g = 1, m_g = 0\rangle$ below T_c . Suppose a mixture of spin 0 and spin -1 particles is formed and cooled below T_c . It can be shown that a very peculiar interaction potential governs the interaction between two spin states below T_c [11]:

$$V_{int} = \frac{4\pi\hbar^2}{3m} \delta(\vec{r}_1 - \vec{r}_2) \cdot \begin{cases} 86a_b & \text{if } F_1 + F_2 = 0 \\ 104a_b & \text{if } F_1 + F_2 = 2 \\ 104a_b & \text{if } F_1 + F_2 = 1 \end{cases} \quad (12)$$

Where a_b is the Bohr radius, \vec{r}_1, \vec{r}_2 are the position of particles 1 and 2, δx the delta function and F the total angular momentum of a particle. From equation 12 several features should be noted:

1. Particles only interact with each other when they directly collide
2. Collisions between $|0\rangle$ and $|-1\rangle$ or $|-1\rangle$ and $|-1\rangle$ particles are energetically unfavourable, while
3. Collisions between $|0\rangle$ and $|0\rangle$ particles (relatively) lower their interaction energy

This leads to the separation of spin states and their formation into large so-called spin domains: macroscopic clusters of a single spin species.

4.2 PCI AND SPIN DEPENDENT PCI IMAGING

Phase Contrast Imaging

Phase Contrast Imaging (PCI) is an optical imaging technique that relies on two principles:

1. To use the real part of the phase induced by a medium to probe its density
2. To use far off resonant light for which the imaginary part of the phase is (very) small

The complex phase acquired by a probe beam passing through a medium can be described as $\phi = \phi' + i\phi''$, where ϕ' represents the phase induced by the medium and ϕ'' represents its optical density. In absorption imaging, the optical density of a medium is probed by calculate the intensity measured by some camera as EE^* and in doing all phase information is lost as the real parts of the complex phase cancel each other out:

$$I \sim E_0 e^{i\phi} E_0^* e^{-i\phi} = |E_0|^2 e^{-\phi''} \quad (13)$$

If we imagine a probe beam to be described by a plane wave $E_{\text{probe}} = E_0 e^{i\phi}$, the electric field of the probe beam after it has passed a cloud of atoms can be represented by

$$E_{\text{transmitted}} = E_{\text{probe}} + E_{\text{atoms}} = E_{\text{probe}} + E_{\text{probe}}(e^{i\phi_{\text{atoms}}} - 1) \quad (14)$$

Here, the field is split into two parts: a part that has been diffracted by atoms inside the gas, E_{atoms} and a part that has not, E_{probe} . The non refracted probe light E_{probe} in 14 represents the plane wave part of the transmitted light. In PCI, the non refracted part of the probe is focused using a positive lens onto a so called phase spot, which phase shifts the plane wave part with a certain phase θ . A second lens is used to focus the light

refracted from the atoms onto a CCD camera. Figure 13 (taken from [8] p.39) illustrates the PCI setup. The electric field can now be represented by

$$E_{\text{transmitted}} = E_{\text{probe}}e^{i\theta_{\text{spot}}} + E_{\text{probe}}(e^{i\phi_{\text{atoms}}} - 1) \quad (15)$$

Due to the far detuning from resonance, the sample will have a negligible optical density. If we assume that the phase spot also has a near zero optical density, the intensity measured by the camera is subsequently given by

$$\frac{I}{I_0} = EE^* = (3 - 2\cos(\theta) + 2\cos(\theta - \phi_{\text{atoms}}) - 2\cos(\phi_{\text{atoms}})) \quad (16)$$

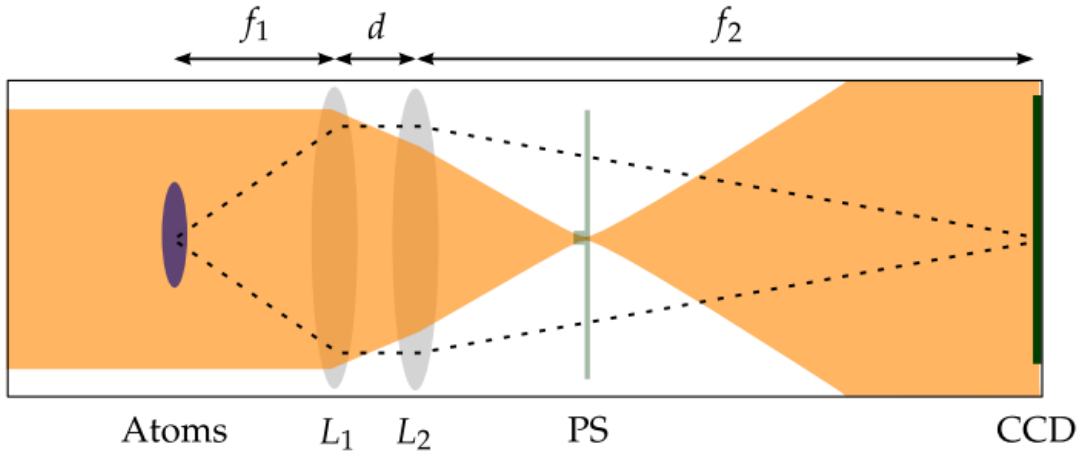


Figure 13.: The plane wave part of the probe beam is focused using a lens onto the phase spot so that only it accumulates a certain phase θ . A second lens focusses the refracted image of the sample onto a camera.

To relate the induced phase to the local density, note that a probe beam propagating through a length l of a medium, will accumulate a complex phase ϕ given by

$$\phi = k(n - 1)l \quad (17)$$

It can be shown that in general, the refractive index n depends on both the density and polarizability of a medium and thus the accumulated phase of a probe beam is given by

$$\phi(x, z) = k \int \sqrt{1 + \frac{\rho(x, y, z)\alpha/\epsilon_0}{1 + C}} - 1 dy \quad (18)$$

With $C = \frac{1}{3}\rho(x, y, z)\alpha/\epsilon_0$. Here, $k = 2\pi/\lambda$, $\rho(x, y, z)$ represents the local density inside the medium, ϵ_0 is the dielectric constant, and α is the polarizability of the medium.

In our application, the imaging of Bose-Einstein condensates formed from sodium atoms, $|\rho\alpha/\epsilon_0| \approx 10^{-2} \ll 1$. The index of refraction can be approximated by

$$n = \sqrt{1 + \frac{\rho\alpha/\epsilon_0}{1 + C}} \approx 1 + \frac{\rho\alpha}{2\epsilon_0} \quad (19)$$

And equation 18 can therefore be simplified into

$$\phi = k \frac{\alpha}{2\epsilon_0} \int \rho(x, y, z) dy = k \frac{\alpha}{2\epsilon_0} \rho_y(x, z) \quad (20)$$

It can be shown[8] that when imaging atoms in a single ground state $|F_g = 1, m_g\rangle$, in the low intensity limit, and with detuning $\delta \ll \omega$ the polarizability α of a gas of atoms is described by

$$\alpha = \frac{i\epsilon_0 c \sigma_\lambda}{\omega} \sum_{g,e} C_{g,e} \frac{\langle F_g, m_g | \hat{\sigma}_{gg} | F_e, m_e \rangle}{1 - i\delta_e/\gamma} \quad (21)$$

Here, δ_e represents the detuning from the $F_g \rightarrow F_e$ transition and σ_λ is the absorption cross section $\sigma_\lambda = 3\lambda^2/2\pi$. For sodium atoms in the $|F_g = 1, -1\rangle$ and $|F_g = 1, 0\rangle$ state equation 21 can be simplified to

$$\alpha = \frac{i\epsilon_0 c \sigma_\lambda}{\omega} \sum_e \frac{D_{F_e}}{1 - i\delta_e/\gamma} \quad (22)$$

In equation 22, the sum runs over all accessible transitions from ground $|F_g = 1, m_g\rangle$ excited state $|F_e = 2, m_e\rangle$ and D_{F_e} represents the relative transition strength shown in figure 14 (calculations done by [7]).

Combining the above, we have a direct relation of the measured light intensity I on a camera, through the complex phase ϕ to the local density ρ of a sample.

Spin Dependant Phase Contrast Imaging

It is clear from equation 22 that at large detuning no single transition dominates in the contribution to the polarizability. From figure 14, it can be noted that in the case of σ_+ light, the sum of transition strengths for the $|F_g = 1, m_g = -1\rangle$ state is 30/60 while for the $|F_g = 1, m_g = 0\rangle$ state it is 40/60. In the case of σ_- light, the sum of transition strengths for the $|F_g = 1, m_g = -1\rangle$ state is 50/60 while for the $|F_g = 1, m_g = 0\rangle$ state it is 40/60. This difference in transition strength directly translates into a difference in the refractive index. We can exploit this difference in refractive index to use phase contrast imaging to non destructively image different spin states.

Using equation 22 and 19, the polarizability and refractive index of the $|-1\rangle$ and $|0\rangle$ states can be calculated for σ_\pm light, and from equation 20 the relative accumulated (real) phase of the two states. The results are listed in table 3. We know from equation 20

State	Polarization	$\sum_e D_{F_e}$	$\text{Re}(\alpha) (10^{-33} \cdot \text{C} \cdot \text{m}^2 \cdot \text{V}^{-1})$	$\text{Re}(n) (\rho \approx 10^{20})$
$ F_g = 1, m_g = -1\rangle$	σ_-	30/60	5.628	1.0320
$ F_g = 1, m_g = -1\rangle$	σ_+	50/60	10.40	1.0594
$ F_g = 1, m_g = 0\rangle$	σ_+ or σ_-	40/60	7.964	1.0453

Table 3.: Refractive Index and polarizability of spinstates using σ_\pm polarized light

and 22 that $\phi \sim \alpha(\delta)\rho_y(x,z)$. If we assume that the detuning to all atomic transitions is large, a condition that can easily be met experimentally, and that the local density is small enough that the accumulated phase ϕ is small for all spin states and polarizations. Expanding equation 16 around $\phi = 0$ the relation between phase and image intensity becomes

$$\frac{I}{I_0} = 1 + 2\sin\theta\phi + \mathcal{O}(\phi^2) \quad (23)$$

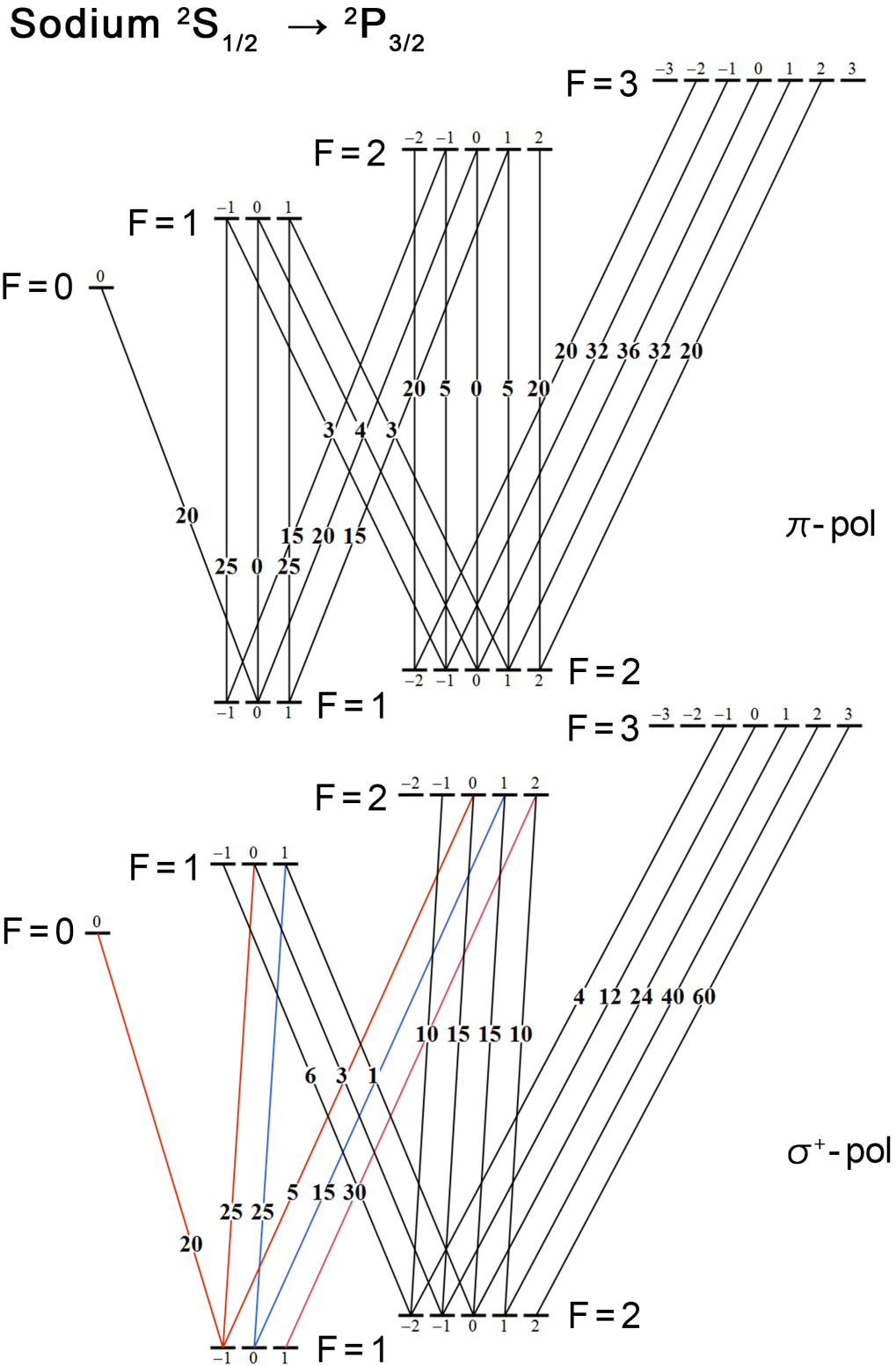


Figure 14.: Transition strengths in the Sodium D2 line used illustrating the concept of Spin Dependant PCI imaging. All transition strengths need to be divides by 60 for the correct normalization. Highlighted in red are the transitions available for $|F_g = 1, m_g = -1\rangle$ states using σ_+ light. Purple show the transitions available for $|F_g = 1, m_g = -1\rangle$ states using σ_+ light. Blue shows the transitions available for $|F_g = 1, m_g = 0\rangle$ states using either σ_+ or σ_- light.

If a linear combination is constructed from two images taken with respectively σ_+ and σ_- polarized light in the following way:

$$\frac{aI_{\sigma_+} - bI_{\sigma_-} - (a - b)}{I_0} = \frac{\sin(\theta)k}{\epsilon_0} (a\alpha_{\sigma_+} - b\alpha_{\sigma_-})\rho_y \quad (24)$$

where a and b are two scale parameters used to multiply the two taken images I_{σ_+} and I_{σ_-} , a new image is constructed that is directly proportional to ρ_y .

By choosing four scale parameters a_0 , a_{-1} , b_0 and b_{-1} , it is possible to construct two separate images each proportional to respectively the density to either the $|-1\rangle$ or $|0\rangle$ states. For the density of $|-1\rangle$ states, we will want a_{-1} and b_{-1} so that

$$\begin{aligned} \frac{\sin(\theta)k}{\epsilon_0} (a_{-1}\alpha_{\sigma_+}^{-1} - b_{-1}\alpha_{\sigma_-}^{-1}) &= 1 \\ \frac{\sin(\theta)k}{\epsilon_0} (a_{-1}\alpha_{\sigma_+}^0 - b_{-1}\alpha_{\sigma_-}^0) &= 0 \end{aligned} \quad (25)$$

Which gives

$$a_{-1} = b_{-1} = \frac{\epsilon_0}{\sin(\theta) (\alpha_{\sigma_+}^{-1} - \alpha_{\sigma_-}^{-1}) k} \quad (26)$$

Similarly for the $|0\rangle$ states

$$\begin{aligned} \frac{\sin(\theta)k}{\epsilon_0} (a_0\alpha_{\sigma_+}^{-1} - b_0\alpha_{\sigma_-}^{-1}) &= 0 \\ \frac{\sin(\theta)k}{\epsilon_0} (a_0\alpha_{\sigma_+}^0 - b_0\alpha_{\sigma_-}^0) &= 1 \end{aligned} \quad (27)$$

Which gives

$$\begin{aligned} a_0 &= \frac{\alpha_{\sigma_-}^{-1}\epsilon_0}{\alpha_0 \sin(\theta) (\alpha_{\sigma_-}^{-1} - \alpha_{\sigma_+}^{-1}) k} \\ b_0 &= \frac{\alpha_{\sigma_+}^{-1}\epsilon_0}{\alpha_0 \sin(\theta) (\alpha_{\sigma_-}^{-1} - \alpha_{\sigma_+}^{-1}) k} \end{aligned} \quad (28)$$

Where α represents the polarizability of spin state -1 or 0 using σ_- or σ_+ polarized light. It follows that by making a pixelwise linear combination of two images I_{σ_+} and I_{σ_-} , one taken using σ_+ light one using σ_-

$$\begin{aligned} \frac{a_{-1}I_{\sigma_+} - b_{-1}I_{\sigma_-} - (a_{-1} - b_{-1})}{I_0} &= \rho_y^{(-1)} \\ \frac{a_0I_{\sigma_+} - b_0I_{\sigma_-} - (a_0 - b_0)}{I_0} &= \rho_y^{(0)} \end{aligned} \quad (29)$$

By using formula 22 to calculate α , and using a $\pi/3$ phase spot, the predicted scaling parameters a and b are found to be:

$$\begin{aligned} a_{-1} &= b_{-1} = 2.01 \cdot 10^{14} \\ a_0 &= -1.42 \cdot 10^{14} \\ b_0 &= -2.62 \cdot 10^{14} \end{aligned} \quad (30)$$

A Python script is used to perform the subtraction process of images. To produce images with significantly improved signal-to-noise ratio, the images are enhanced using an IDL routine that utilizes a Singular Value Decomposition (SVD) technique to extract stationary (or the converse, non stationary) features from a series of images while eliminating all changing elements allowing a foreground and background part of an image to be distinguished. Using SVD, sections of the images not containing any image of the atomic sample are (manually) marked off as 'background' sections. The SVD routine will then attempt to construct a linear combination all these background images representing the background of a current image and subsequently subtract it. Defects such as interference patterns can be removed to a high degree using this technique.

4.3 ROTATING THE QUANTIZATION AXIS

For the subtraction technique to have maximal contrast, atoms need to be probed using σ_+ and σ_+ light. This means the quantization axis of the spin states, i.e. the background magnetic field in our experiment, needs to be parallel to the probe beam k vector. In our experimental setup, ordinarily the magnetic field is directed into the $+\hat{z}$ direction for the purpose of creating domains of spin polarized particles using the Landau-Zener mechanism with a RF sweep. For our technique to work, we therefore need to turn the magnetic field towards the \hat{y} direction.

To achieve this, a magnetic field in the $+\hat{y}$ direction is gradually switched on to 3.4G in 500ms using the \hat{y} -compensation coils, while simultaneously decreasing the initial magnetic field components in the \hat{z} direction to zero by decreasing the MOT and Bias coil currents in the same time interval. As a result, the magnetic field strength is not constant during the rotation, but for experimental purposes only the direction of the magnetic field matters, not its strength. We measured the earth magnetic field in our lab to be $H_{\text{Earth}} = (-0.41, 0.61, 0.00)\text{G}$. By applying the \hat{y} field, the resulting magnetic field vector is angled 5° to the \hat{y} axis and pointing slightly into the $-\hat{x}$ direction.

As an experimental verification that the rotation of the quantization axis was successful and that atoms are still in the $|F_g = 1, m_g = -1\rangle$ state relative to the now rotated quantization axis, the following experiment was performed. A sample of atoms in the $|F_g = 1, m_g = -1\rangle$ state was prepared. Chapter B shows that the dependency of the atomic transition strength of the $|F_g = 1, m_g = -1\rangle \rightarrow |F_e = 1, m_e\rangle$ on the polarization state of the probing light using half and quarter wave plates in the $\vec{H} \parallel \hat{z}$ and $H \parallel \hat{y}$ settings are given by:

$$\mathcal{D}_{\lambda/2}^{H_z} = \frac{5}{48} (3 - \cos(4\theta)) \quad (31)$$

$$\mathcal{D}_{\lambda/4}^{H_z} = \frac{5}{96} (5 - \cos(4\theta)) \quad (32)$$

$$\mathcal{D}_{\lambda/2}^{H_y} = \frac{5}{24} \quad (33)$$

$$\mathcal{D}_{\lambda/4}^{H_y} = \frac{5}{24} (1 + \sin(2\theta)) \quad (34)$$

Here, θ represents the angle at which a wave plate has been rotated around its axis. Polarized light and the transition strength thus provides a tool to measure the degree to which the change of the quantization axis was successful. The atomic sample was imaged using absorption imaging on the $|F_g = 1, m_g = -1\rangle \rightarrow |F_e = 1, m_e\rangle$ transition using

a quarter and half wave plate in both the $\vec{H} \parallel \hat{z}$ and $H \parallel \hat{y}$ settings. The results are shown in figures 16 and 15. Even though the absorption of σ_- light does not go to zero completely and the absorption of linear light is not completely constant over all polarization angles, we conclude that the change of the quantization axis is successful to a large degree. By rotating the magnetic field, the contrast difference for absorption of σ_{\pm} light $OD_{\sigma_+} - OD_{\sigma_-}$ has increased from 0.25 to 0.5.

4.4 CREATING σ_+ AND σ_- POLARIZED LIGHT

Our spin dependant PCI technique uses two images of a sample taken with σ_{\pm} light. For the technique to be successful, we need to be able to quickly switch between σ_- and σ_+ light. To quickly switch between these light polarization states, we use a Thorlabs LCC1112-A liquid crystal waveplate and a LCC25 liquid crystal controller. By applying a voltage using the LCC25, an electric field changes the orientation of the nematic crystals inside the device, which changes the birefringent properties of the waveplate. Together, the LCC1112 acts as a voltage controlled waveplate capable of creating a phase retardance slightly over $3/4\lambda$.

As the phase retardance of the LCC is wavelength and temperature dependant, we use a simple procedure to determine the $\lambda/4$ and $\lambda/4$ voltage. The setup and results are shown in figure 17 and 18. Using figure 18 and the knowledge that increasing the electric field strength decreases the retardance, $V_{\sigma_+} = 3.97$ and $V_{\sigma_-} = 1.70$

Switching time between two polarization states depends on the temperature of the controller, the voltage difference between the two states and the direction of the switch. Switching from a high to a low voltage is slow, switching from a low to a high voltage around a factor 6 faster. By connecting the power meter to an oscilloscope and setting the temperature of the controller to 45°C a slow switching time of 25ms is measured for a 100% switch to be made from voltage V_2 to V_1 . However, after 15ms 90% of the polarization state has been changed to circular light, and to be able to take images at full speed we will use 15ms our preprogrammed switching time for taking images. The fast switching time (V_1 to V_2) is less than 5ms.

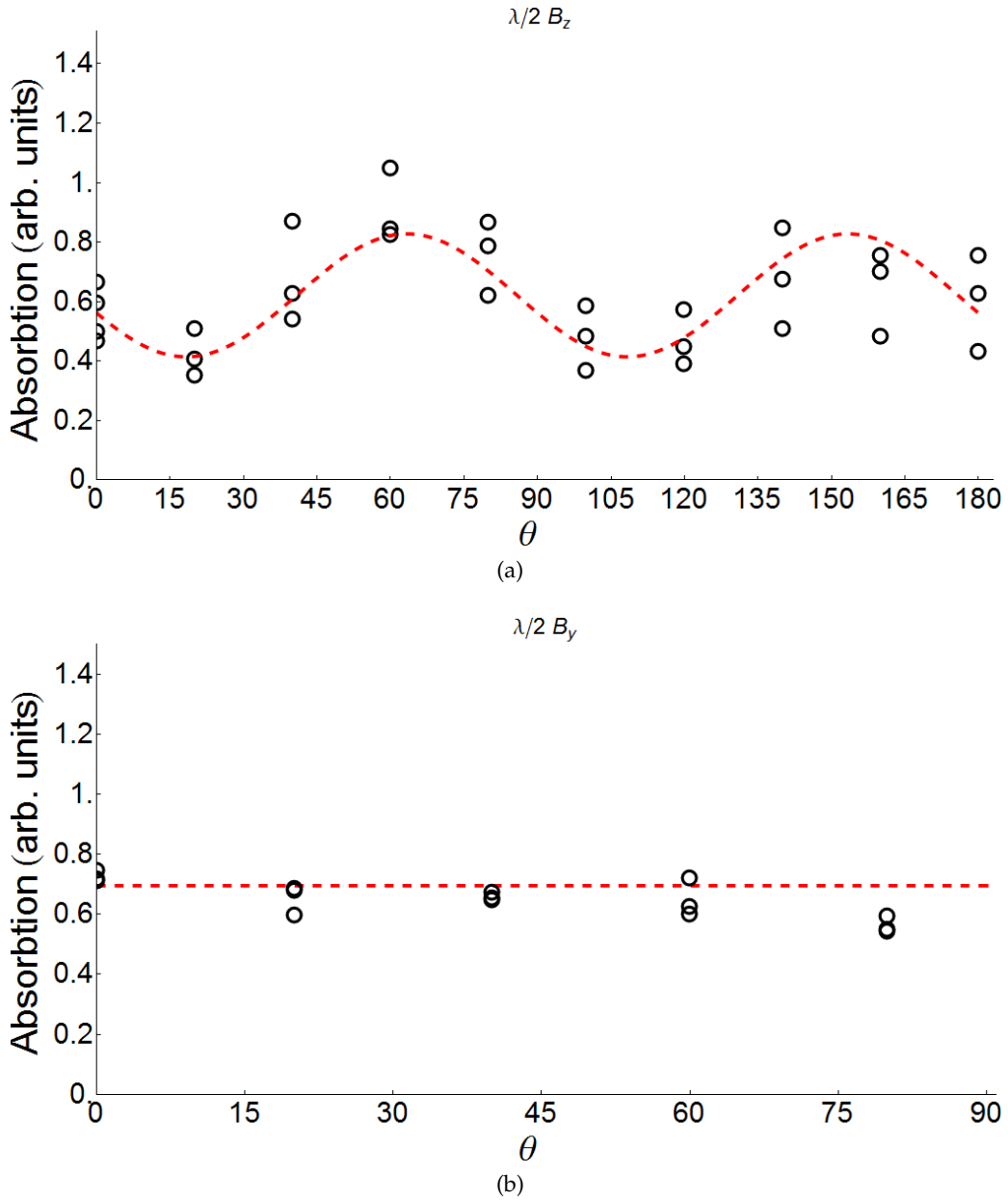


Figure 15.: Measurement of absorption on the $|F_g = 1, m_g = 1 \rightarrow F_e = 1, m_e\rangle$ transition as a function the polarization state of probing light by rotating a half wave plate over an angle θ . In (a) the magnetic field is orientated along the \hat{z} axis, in (b) the field is orientated along the \hat{y} axis. Shown in red it a fit using the transition strengths from 31 and 33 Measurement (a) is most likely not reliable, as the liquid nitrogen cooling used to keep the vacuum conditions during experiments at an optimal level was almost depleted. A decrease in absorption or higher spread in the measured absorption could also be caused by a smaller condensate lifetime.

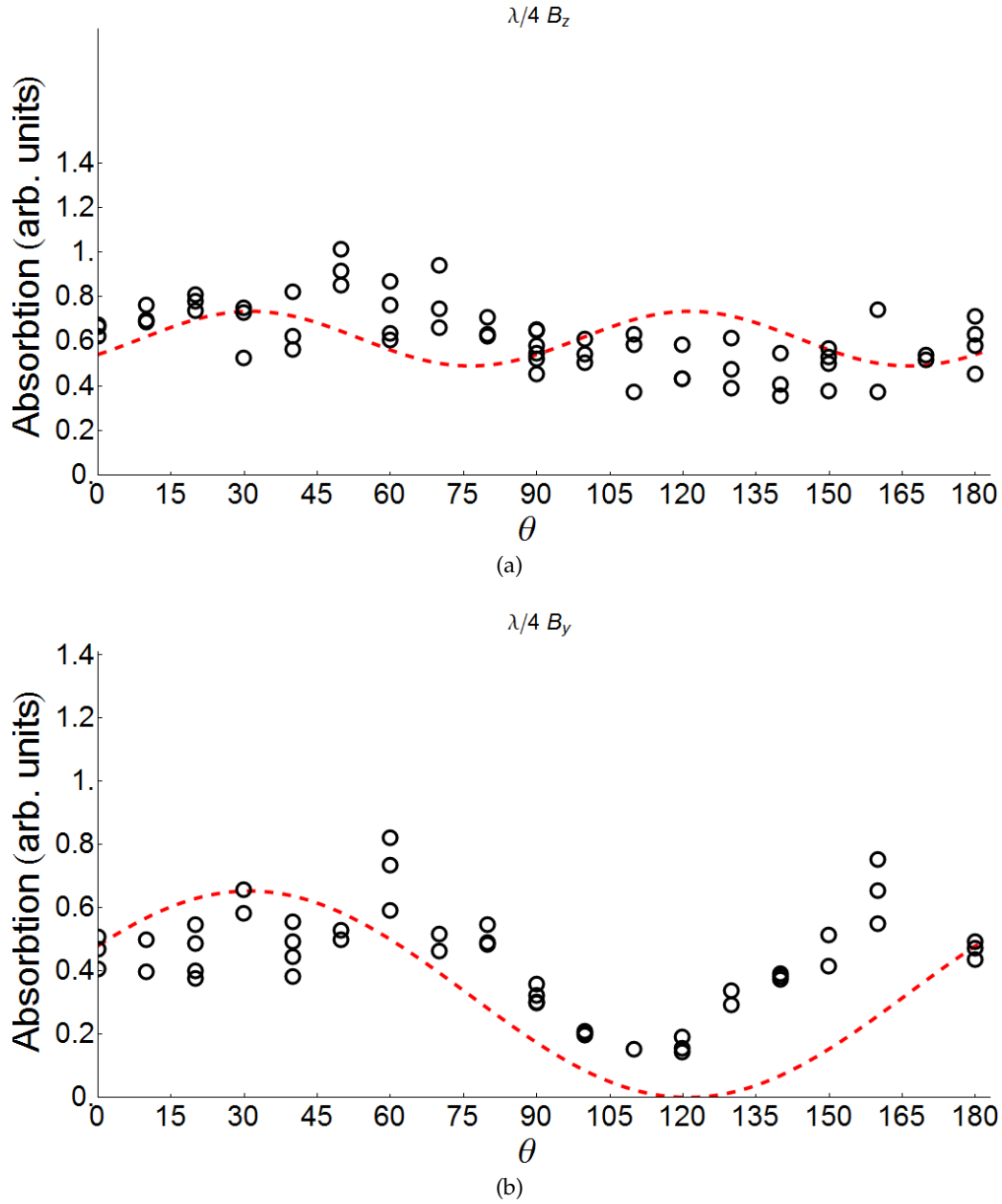


Figure 16.: Measurement of absorbion on the $|F_g = 1, m_g = 1 \rightarrow F_e = 1, m_e\rangle$ transition as a function the polarization state of probing light by rotating a quarter wave plate over an angle θ . In (a) the magnetic field is orientated along the \hat{z} axis, in (b) the field is orientated along the \hat{y} axis. Shown in red it a fit using the transition strengths from 32 and 34

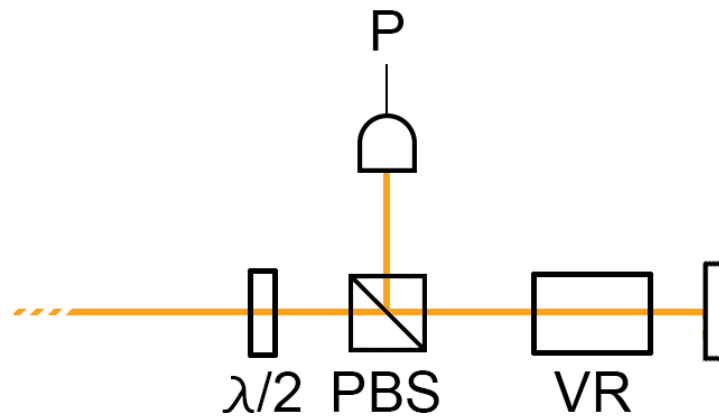


Figure 17.: Light is linearly polarized using a $\lambda/2$ waveplate and a PBS. Light is double passed through the LC1112 (VR) using a zero angle of incidence mirror. The fast axis of the VR is set to 45 degrees relative to the P polarized light from the PBS. When the transmission to the powermeter P is maximal, the VR acts as a $\lambda/4$ or $3\lambda/4$.

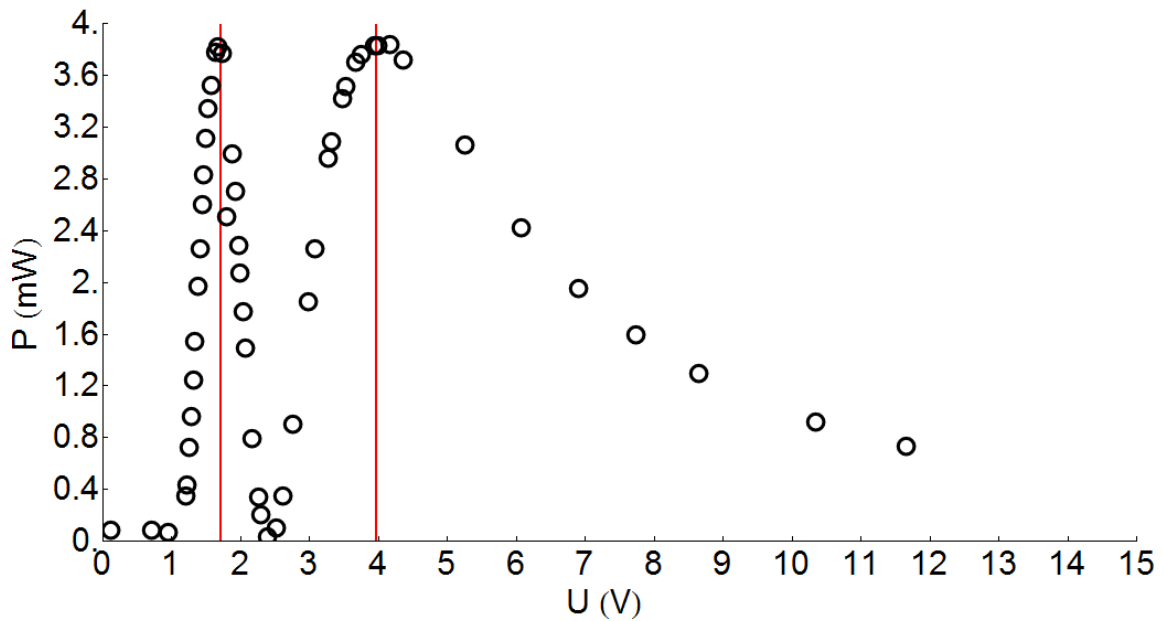


Figure 18.: Measured reflected power from the PBS. The two peaks represent the two voltages at which the LCC acts as a $\lambda/4$ and $3\lambda/4$ respectively

Non Destructive Spatial Imaging of Spin Domains

5.1 EXPERIMENTAL RESULTS OF SPIN DEPENDENT PCI

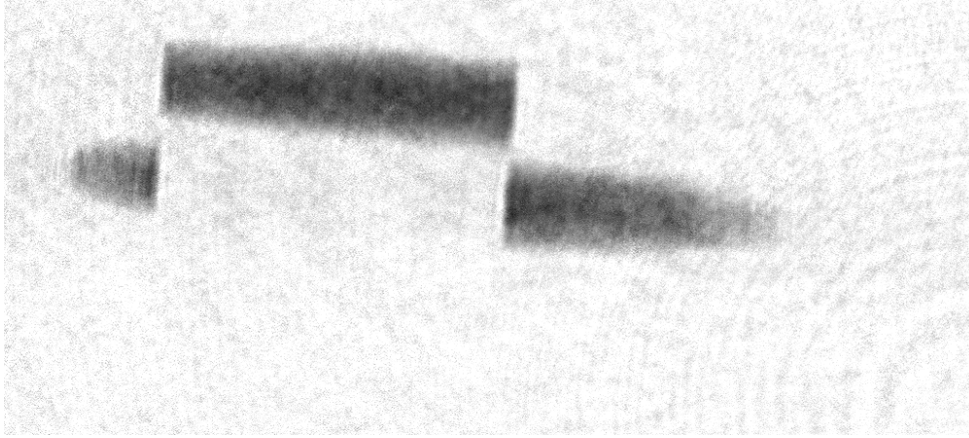
FORT trapping frequencies were not precisely determined, but based on the used FORT beam power and previous estimates of the focal size in similar experimental conditions we estimate them to be in the order of 1.5 Hz axial and 220Hz radial. Once atoms are loaded into the FORT, a RF sweep in 20ms with from 2 to 4 Mhz is used to spin polarize atoms into two states, $|F = 1, m = -1\rangle$ and $|F = 1, m = 0\rangle$, with respect to a magnetic field of 3.7G in the $+\hat{z}$ direction created using 2.1A sent through the MOT coils. When the sample is cooled below T_c , three large separated domains are formed of spin states $|0\rangle, |-1\rangle$. Figure 19 shows the formed domains using absorption on the $F_g = 1 \rightarrow F_e = 1$ transition after 5ms expansion using time of flight. To maximize the transition strength while using absorption imaging, a magnetic field 5.3G is created in the $+\hat{z}$ direction using the fine tune coils, pulling the magnetic quantization axis into the same plane as the polarization vector of the (linear) probing light.

We noticed a feature that we as of yet do not fully understand. In an attempt to let the quantization axis be aligned along the \hat{y} axis before atoms are cooled to below to T_c (i.e. to skip the rotation step) we observed that the formed spin domains were completely different from those formed with the quantization axis in the \hat{z} direction. Where in the \hat{z} setting, three large domains are formed, in the \hat{y} setting many small vertical domains in a stripe pattern are formed. An image using absorption imaging is shown in figure 19. As the FORT trapping potential is symmetrical around its long axis in the \hat{z} direction and no other fields were present to our knowledge, we don't have an explanation as to why the domains form this way.

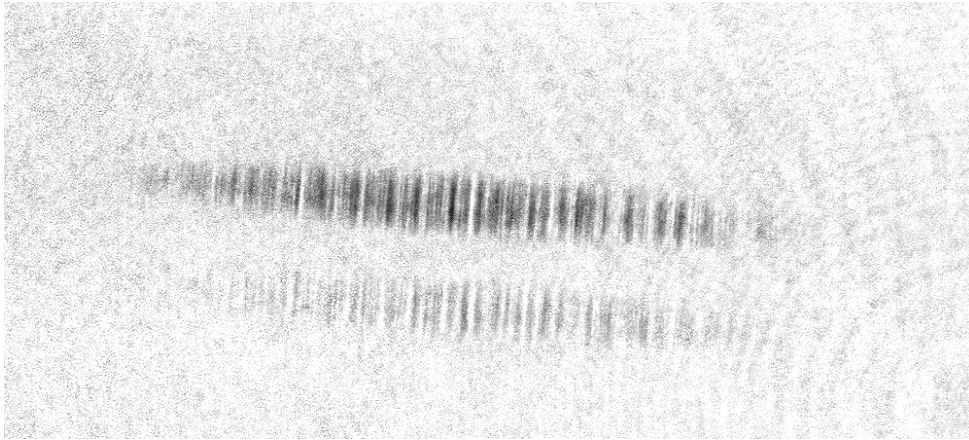
To perform Spin PCI, the LC1112 is set to 45°C and the σ_+ and σ_- voltages are preset into the LCC25 ready to be triggered using a digital control channel from the Wordgenerator. A phase spot of $\pi/3$ is used with a probe that is detuned $\delta = -346$ Mhz from the $F_g = 1 \rightarrow F_e = 1$ transition. Once the atomic sample has been spin polarized into two spin states, the magnetic field is rotated into the \hat{y} direction (see chapter 4.3) in 500ms by gradually switching on a 3.4G field.

Two images are taken 15ms apart, one using σ_+ light, the other using σ_- light. A Python script is used to subtract the images from one another. A resulting image is show in figure 20.

It was found that the calculated subtraction parameters a and b from section 4.2 did not produce pictures where either only $|-1\rangle$ or $|0\rangle$ were visible. By trying different scaling



(a)



(b)

Figure 19.: (a) Three large separated spin domains of spin states $|0\rangle$, $|-1\rangle$, and $|0\rangle$ using a quantization axis in the \hat{z} direction and the Stern-Gerlach splitting principle

(b) Spin domain texture formed with the quantization axis in the \hat{y} direction and the Stern-Gerlach splitting principle. Domains still consist of $|0\rangle$ and $|-1\rangle$ states, although the domain structure is drastically different from the \hat{z} quantization axis setting

parameters, the following parameters were found to produce images where only a single spin species is visible. For the initials, non-SVD converted images:

$$\begin{aligned} a_{-1} &= 2.30 \\ b_{-1} &= 1.70 \end{aligned} \tag{35}$$

$$\begin{aligned} a_0 &= -1.70 \\ b_0 &= -2.60 \end{aligned} \tag{36}$$

For the images used to determine the spin drag rate (see section 5.2), the scaling parameters were:

$$\begin{aligned} a_{-1} &= 1.75 \\ b_{-1} &= 1.65 \end{aligned} \tag{37}$$

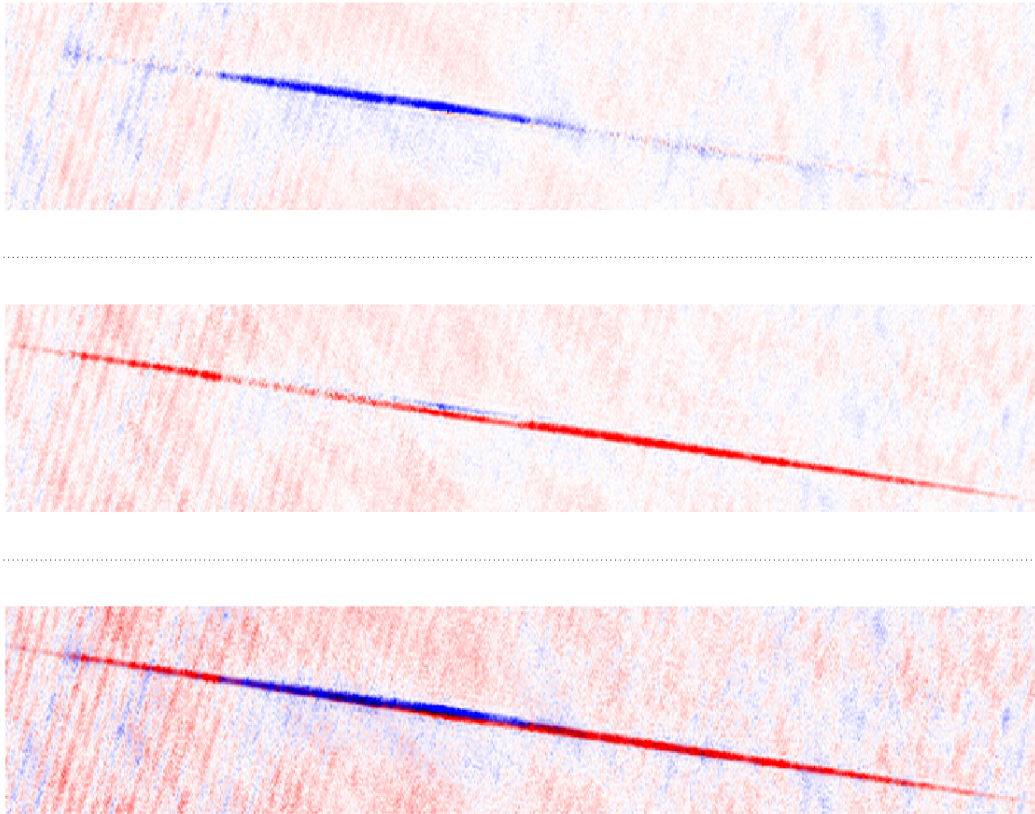


Figure 20.: Top: $| -1 \rangle$ density in blue, using $a_{-1} = 2.30$ and $b_{-1} = 1.70$. Middle $| 0 \rangle$ density in red, using $a_0 = -1.70$ and $b_0 = -2.60$. Bottom: combination of both $| -1 \rangle$ or $| 0 \rangle$ densities.

Coloring is done by assigning a positive numerical value to $| 0 \rangle$ densities and a negative value to $| -1 \rangle$ densities and using a function that assigns a CMYK color to each pixel accordingly. Combination of images is then a simple sum of colors per pixel, resulting in a blended purple when both spin types are present.

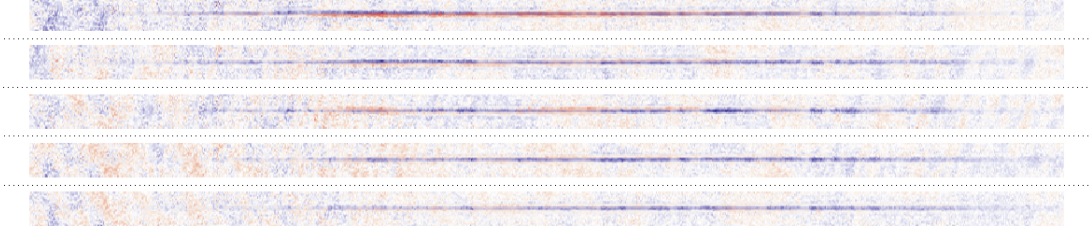


Figure 21.: 5 in-situ spin dependant PCI images shot 15ms apart to check FORT movement or vibrations. The images are enlarged by a factor 1.5 in the y direction for clarity. Very slight scissor movement can be seen in the first image.

$$\begin{aligned} a_0 &= -1.46 \\ b_0 &= -2.17 \end{aligned} \quad (38)$$

Although these parameters produce spatially correct images, they give no guarantees about the local density.

Because movement or vibration of the FORT would significantly reduce reliability of the Spin PCI images by possibly subtracting incorrect image parts from each other, multiple images using only $|-1\rangle$ particles were taken to establish the extent of the FORT movement. An example image is shown in figure 21. Although no in depth analysis of the stability of the FORT was conducted, it was concluded from the images that the FORT could move up to 3 pixels in the radial direction during a scissor like movement, but that given the pixel width of the BEC in situ was 10 pixels this would not prevent the detection of domains of different spin species.

5.2 APPLICATION: SPIN DRAG BELOW T_c

Having created an imaging technique to non destructively image spin states, we wish to test the technique in a proof-of-concept experiment.

Our research group has recently done experiments on the phenomenon of spin drag: a drag force experienced by spin domains that are forced to move through each other. To induce a force on a particle of a certain spin type, we use a magnetic gradient force:

$$F_{\text{MOT}} = m x''(t) = g_F m_F \mu_B \frac{d\vec{B}(\vec{r})}{dz} \quad (39)$$

Here, g_F is de Landè g-factor ($= -\frac{1}{2}$, see [12]), μ_B is the Bohr magneton, m the mass of a sodium-23 atom, and m_F the magnetic moment of a spin particle. We thus immediately see that by applying a magnetic gradient, we can selectively exert a force on $|-1\rangle$ state particles and leave the $|0\rangle$ state particles untouched. By using a combination of MOT and fine tune coils, we are able to create a homogeneous magnetic gradient (around the FORT center) into the \hat{z} direction.

As a qualitative model for spin drag, we use a classical model of friction, with boundary conditions $\Delta x(-15ms) = d$ and $\Delta x'(-15ms) = v_0$

$$\Delta x''(t) + 2\gamma \Delta x'(t) + \omega^2(\Delta x + \Delta x_0) = \frac{F_{\text{MOT}}}{m} \quad (40)$$

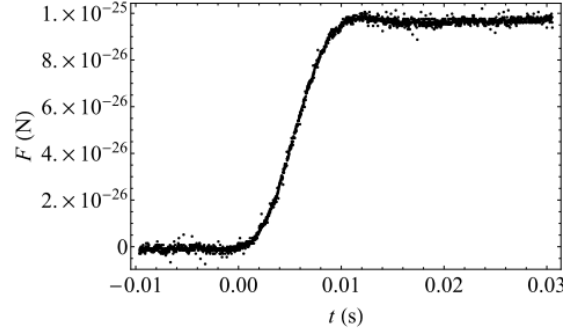


Figure 22.: Applied magnetic force as a function of time as measured by [5]

Here, γ is the spin drag coefficient and Δx is the distance between the center of masses of the two spin domains being pulled through one another and $\omega^2(\Delta x + \Delta x_0)$ accounts for the shape of the FORT trapping potential. Ideally $\Delta x'(-15ms) = 0$, as the spin domains are initially stationary. We choose to take images 15ms after the magnetic gradient force is switched on to eliminate any self induction effects that might arise when the MOT coils are switched on and result in a time dependent force being applied to the spin domains. Figure 22 shows the time dependence of the magnetic gradient force as measured by [5]. Because our axial trapping frequency is only in the order of 1.5Hz and particles can therefore move relatively unrestricted in the axial direction, we will neglect the trapping potential part from equation 41. The solution to equation 41 then looks like:

$$\Delta x(t) = \frac{e^{-2t\gamma_m} (e^{2t\gamma_m} (2\gamma_m (2d\gamma_m + v_0) + F_{\text{MOT}} (2t\gamma_m - 1)) + F_{\text{MOT}} - 2v_0\gamma_m)}{4\gamma_m^2} \quad (41)$$

Where v_0 represents the initial velocity of the domains and d the initial center of mass separation.

Once atoms are loaded into the FORT, the sample is spin polarized and cooled to below T_c as described in section 5.1. Different magnetic dragging forces are applied to the atoms. 20 images are taken in a single image series, alternating between σ_+ and σ_- light with a repetition rate of 15ms. Noise is eliminated from the images using the SVD routine, and the σ_+ and σ_- images are processed using a Python script. Figure 23 shows an example of a image series measured at $F_{\text{MOT}} = 0.48 \cdot 10^{-24}N$. To find the center of mass of the spin -1 and spin 0 spin domains and reduce noise, the image part containing atoms is cut out and summed into bins in the vertical image direction. Bin values below a certain threshold value are assumed to be zero. The remaining bins are assumed to represent the condensate fractions and the center of mass is calculated by taking the weighted average over all bins. Figure 25 shows an example of a y-summed image.

A measurement series using different drag forces is performed. The fitting curves are shown in figures 26a and figure 26b shows the estimated γ_m per measurement. By taking the weighted average of the estimated γ_m values, we find as a $\gamma_m = 147 \pm 16s^{-1}kg^{-1}$.

When looking at the optical density of the imaged sample, we see that the optical density decreases as a function of the applied magnetic force. When looking at the rate the relative optical density decreases with time, we see that this rate is lower for the cases in which a high magnetic gradient force is applied. Figure 27 shows the optical density as a function of the applied magnetic force.

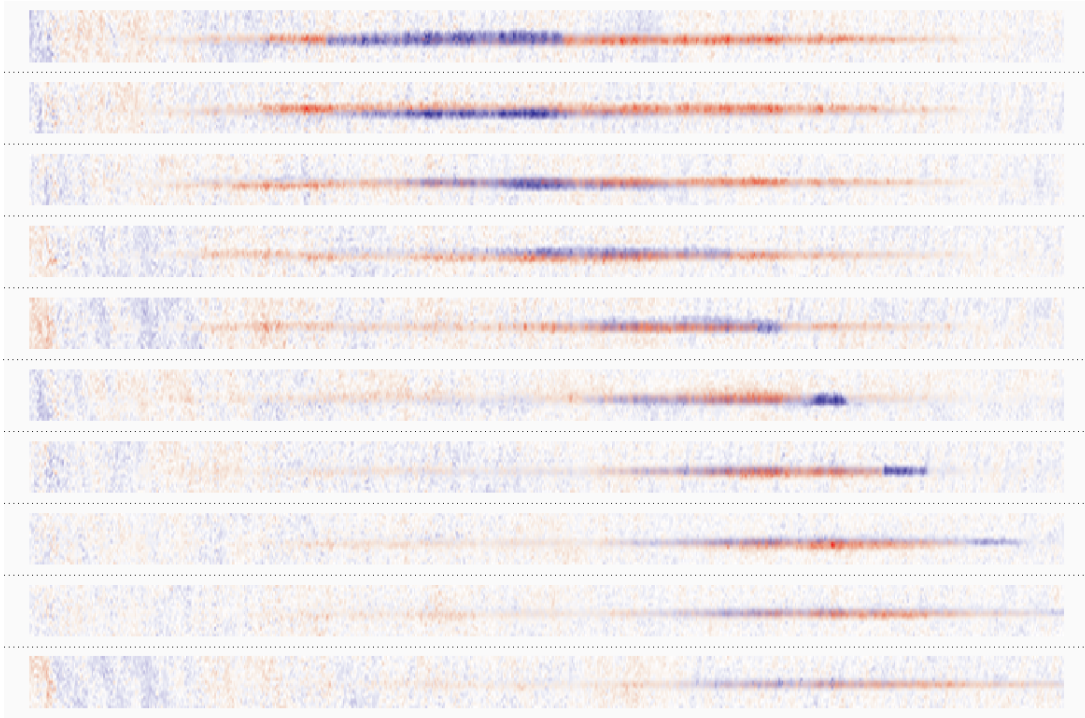


Figure 23.: Image series after SVD of spin drag measurement at $F_{\text{MOT}} = 0.48 \cdot 10^{-24}N$. Images are 30ms apart. We see the central blue spin -1 particles move to the right, move past the red spin 0 particles and emerge on the other side after which they escape

1

5.3 DISCUSSION

Experimental determination of γ_m

We have succeeded in imaging spin states using non-destructive PCI using two images with σ_+ and σ_- light and have demonstrated that we are able to spatially image individual spin domains at a rate of 33.33 fps using two images taken 15ms apart using respectively σ_+ and σ_- light. Here, several of the results will be discussed together with some remarks about the spin PCI technique.

Our drag rate consistent with the measurements done by Ref [5]. Although we are confident that our measurement is at least qualitatively correct, some remarks can be made. Accuracy of the measurements could be improved if the atoms in the MOT are initially polarized into two symmetric spin domains, instead of a central spin -1 domain surrounded by spin 0 parts. In the latter case, the center of mass of the spin 0 domain is less sharply defined and therefore Δx is less accurate. By creating two separate parts, it will also take longer for the spin -1 particles to reach the right hand side of the FORT,

¹ Deteriorating experimental conditions could be loss in FORT power or because the old dye laser setup (see [8]) was still being used for the Zeeman slowing process. A decrease in power from the Zeeman slower dye laser due to drift of the frequency lock or deteriorating quality of the dye itself would lead to lower numbers of starting particles.

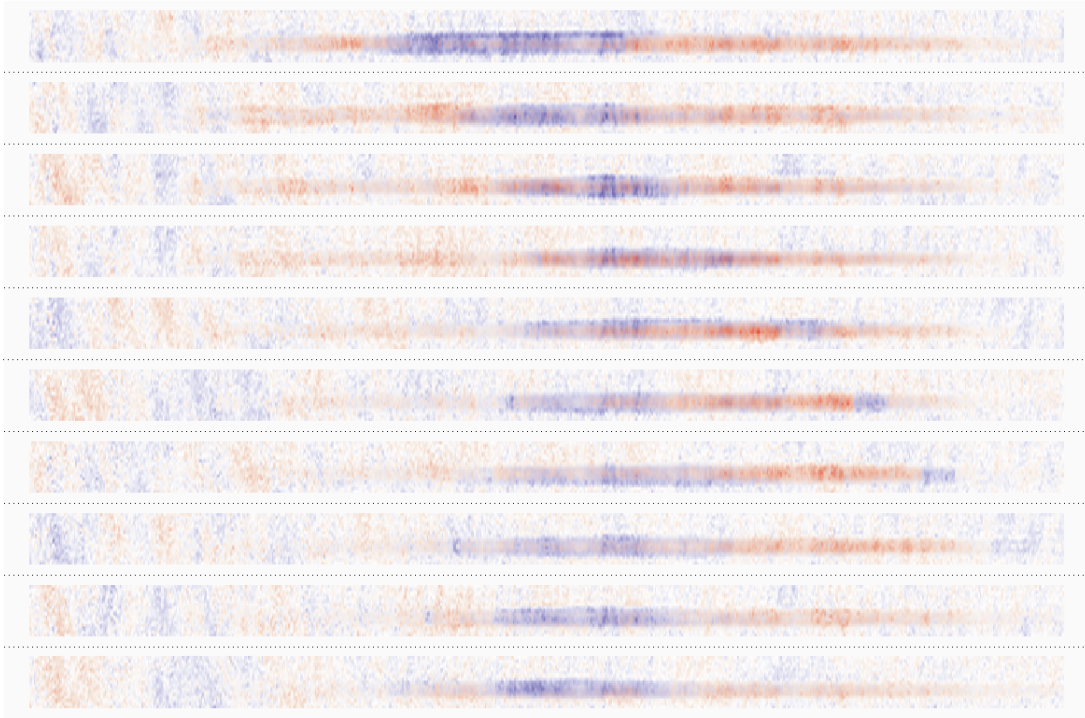


Figure 24.: Image series after SVD of spin drag measurement at $F_{\text{MOT}} = 1.08 \cdot 10^{-24}N$. Images are 30ms apart. We see the central blue spin -1 particles move to the right at a high speed, avoiding the 0 particles and emerge on the other side after which they escape. Note the distinct lower contrast of the image as the applied magnetic field in the \hat{z} direction causes the magnetic quantization axis to no longer be pointed directly into the $+\hat{y}$ direction.

resulting in more data points that can be used for fitting.

The remaining part of what appears to be $|-1\rangle$ state particles in the center of the FORT remain as of yet unexplained. Perhaps the density of $|0\rangle$ is too high for the $|-1\rangle$ particles to be able to push through, effectively forming a blockade inside the trap, but this is pure speculation. More experimental investigation, as is the case for the striped spin texture from image 19, is needed to come to a satisfactory conclusion.

Repetition Rate

The imaging setup could be further improved if images were taken at a higher repetition rate. In most image series, $|-1\rangle$ state particles begin reaching the righthand side of the trap and escape after 165ms or 5 images. The switching time is in the first place limited by the variable retarder to at least 15ms. If a faster switching time was possible, not only would measuring the drag rate be easier by creating more data points, it would also decrease any possible image smear as the σ_+ and σ_- images being subtracted are closer together in time. Although the extent to which image smear is a factor currently seems to be limited (but has not been thoroughly determined), image smear in the measurement of the spin drag rate would not prevent the determination of the center of mass as the spin domains move at a mostly constant velocity and so any smear is symmetrical for the two taken images.

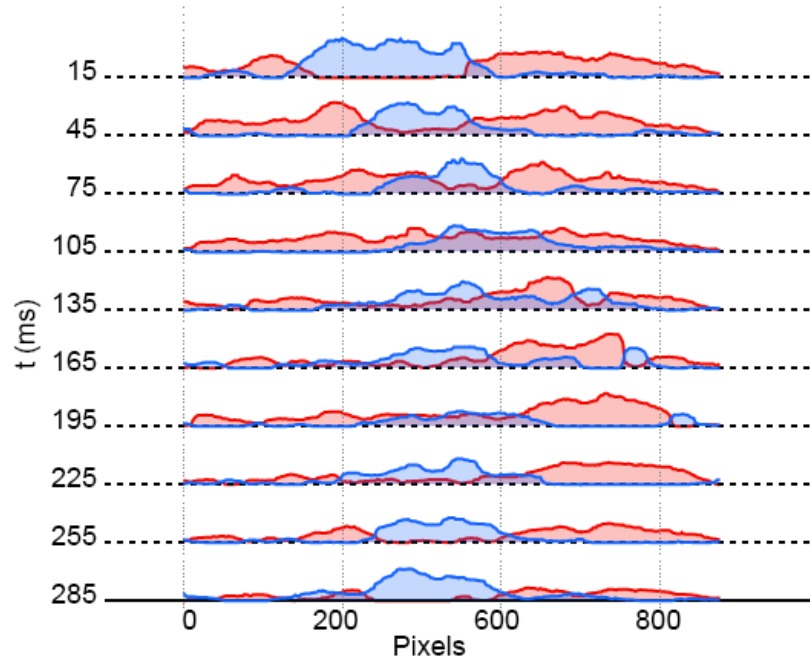


Figure 25.: Summation of pixels in the y-direction of figure 24 for extra clarity. A 20 pixel rolling median filter is applied to the bin values to produce a slightly smoother image. Y-summed images are used to find the center of mass for spin -1 and spin 0 particles by taking the weighted average along the x direction. From this image, it can clearly be seen that a block of what appears to be spin -1 particles is left in the center of the trap at the end of a measurement. Why it is left is not understood.

A higher imaging rate could be achieved by replacing the variable retarder with a Pockels cell. A Pockels cell can achieve switching times in the order of several nanoseconds. Considerations to be made would be the additional optics required and adjustments in the experimental setup for the probe beam, as a Pockels cell in general has a small clear aperture and we require a relatively large probe beam waist diameter. To take full advantage of any improvements in the polarization switching time, the readout time of the camera used for imaging also needs to be improved. Currently the camera is operated in single shot mode, but if the camera is operated in crop mode imaging rates of up to 0.5-1ms should be achievable.

Scaling Parameters and \vec{H} field

Some remarks on the Spin PCI technique itself can be made. Firstly, it is not known why the scaling parameters a and b differ so much from the predicted value, and also between two separate imaging series. From the images in figure 27, we conclude that using a magnetic gradient force to drag our spin domains most likely pulls the magnetic field vector away from the \hat{y} direction which results in probing the atomic sample with an unknown superposition of σ_+ , σ_- and π polarized light. The fact that the magnetic field is not directed purely along the y-axis might explain why the predicted scaling parameters do not correspond with the ones found by hand.

As a possible idea to study the direction of the magnetic field, one could use rotation matrices for rotations along the \hat{x} , \hat{y} and \hat{z} axes in conjunction with the Jones matrices

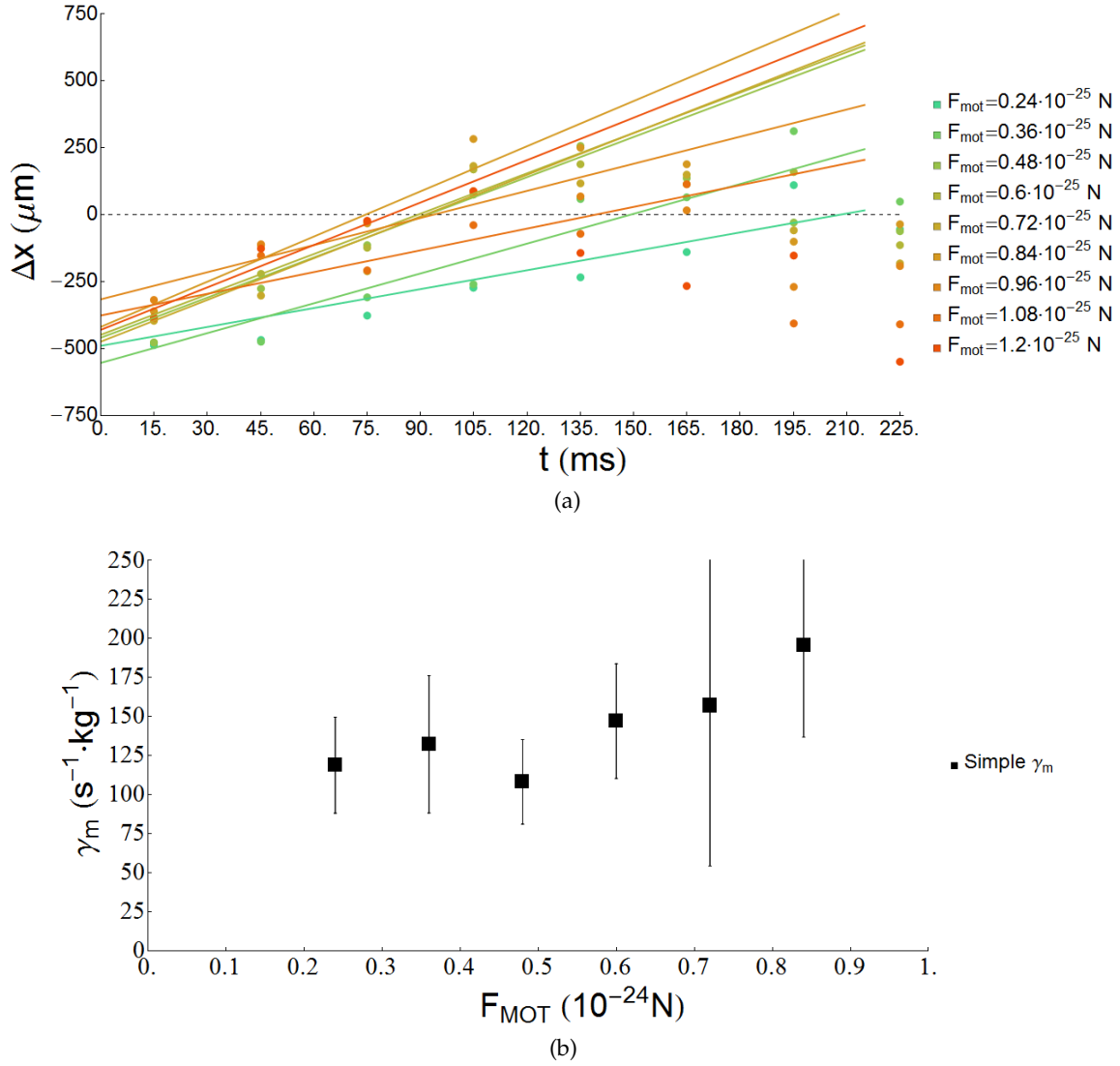


Figure 26.: Separation Δx of the center of masses for spin domain of $|-1\rangle$ and $|0\rangle$ state atoms over time at different applied magnetic forces. (a) shows the simple model from 41. In general, Δx increases with time, meaning that the center of mass of the spin domains are pulled past each other. After around 5 images are taken in a series, the $|-1\rangle$ domain reaches the right hand side of the trap and is able to escape, thereby causing the center of mass to move back towards the center again. (b) shows the estimated γ_m as a function of the applied magnetic force for both the model with and without induction.

to calculate the polarization dependent transition strength as a function of a magnetic field that is directed along an arbitrary direction. It might then be possible to find the orientation of the magnetic field, by measuring the dependence of the transition strength as a function of the polarization state, in similar fashion as was done in section 4.3.

Varying the magnetic field strength in the \hat{y} direction and doing absorption imaging (again as a function of polarization), could also give insight into the orientation of the magnetic field.

It should be noted that, potentially, a strong magnetic gradient might even result in a spatial dependence of the polarizability of the atoms trapped inside the FORT. To counter any unwanted effects of applying a magnetic gradient force, a stronger magnetic

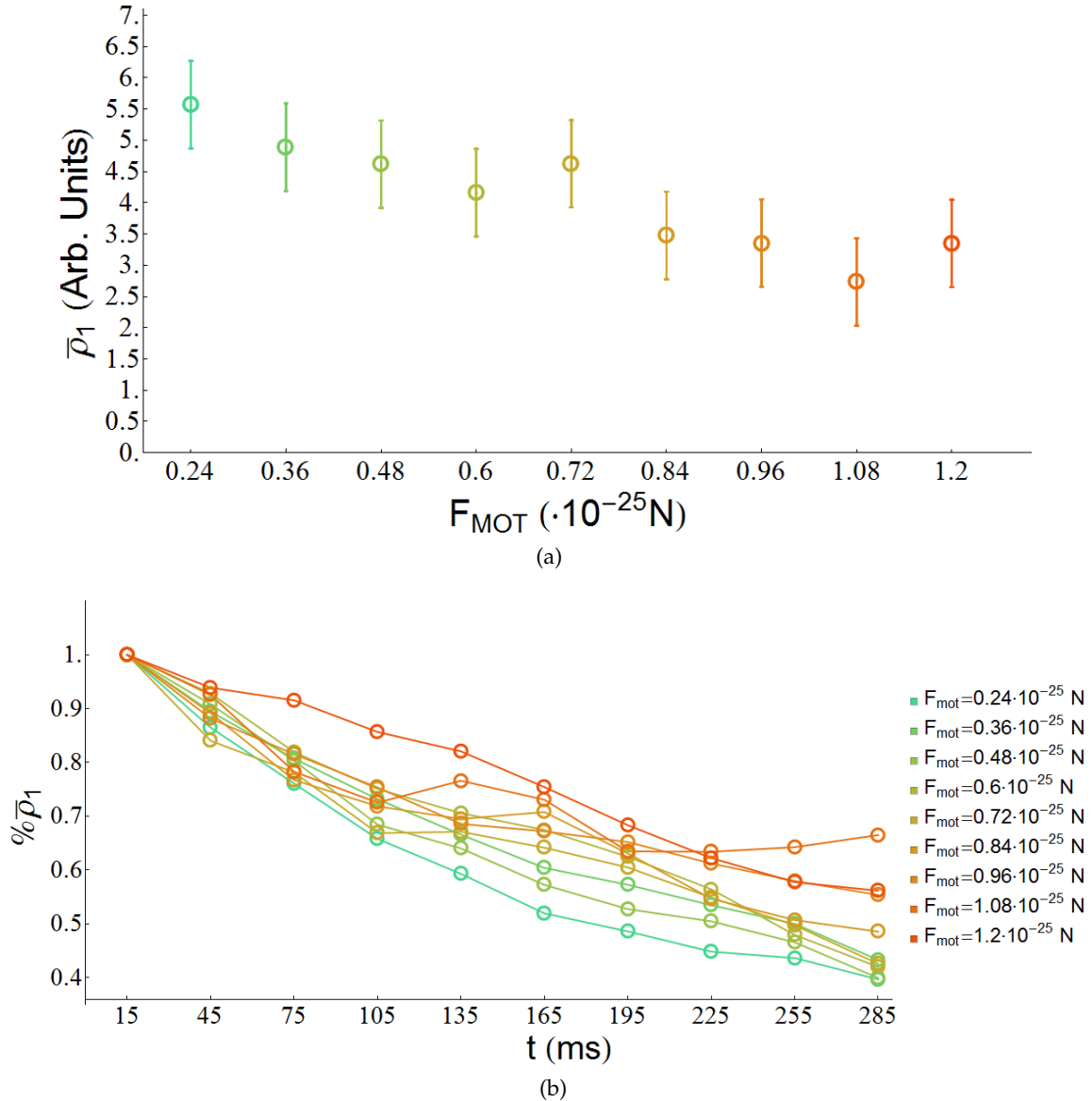


Figure 27.: (a) Measured mean optical density in the first image of a spin drag measurement as a function of the applied magnetic force. Higher magnetic forces shift the quantization axis so that the sample is no longer probed with pure σ light. The full extent of this effect is not known yet as a true decrease in optical density, due to deteriorating experimental conditions during the measurement series, cannot be ruled out because the images were taken in chronological order.

(b) Relative density over time plotted against the applied magnetic force. We see from the image that the rate at which the optical density decreases is less for a higher applied magnetic field. This suggests that when a strong magnetic field in the \hat{z} direction is applied, the transition strength decreases due to probing with non σ polarized light.

field component in the \hat{y} direction could be created by wrapping more coil windings around the experimental setup. Conversely, lowering dragging forces and longer measuring times could also provide a solution.

Another possible factor could be that the fast switching time of 15ms using the variable

retarder during the drag rate measurement is not long enough to produce pure σ_- or σ_+ polarized light. The transition strengths for elliptically polarized light would differ from circular light and would not be (anti)symmetrical when switching from righthanded to lefthanded elliptical light for both $|0\rangle$ and $|-1\rangle$ states, leading to skewed scaling parameters a and b .

Because the scale parameters for the image subtraction were found by hand, presently they give no guarantee that ρ is 1-to-1 proportional to the measured intensity. Although this poses no problem in the determination of the center of mass, the scaling factors need to be accounted for if applications requiring the absolute density are desired. A series of calibration measurements, by imaging only a single particle species using both spin dependent PCI and absorption imaging, could be used to experimentally determine the factors a and b and possibly also rule out any dependence on the switching time of the variable retarder.

Future Improvements of the Experimental Setup

As a more general limitation, equation 23 only works when imaging a sample at a low enough densities such that the accumulated phase ϕ is small. If we were to image samples at a higher density, intensity would no longer scale linearly with phase. For high densities measurements, we therefore need to be able to detune the probe further. Using a voltage controlled offset lock for the probing ($F=1$) laser, relative to the MOT and cooling ($F=2$) laser, could solve this problem by being able to detune the probing laser to any frequency so desired.

Although vibrations of the FORT did not prevent us to determine the center of mass of the spin domains, FORT vibrations could be a source of measuring errors, as a scissor mode might wrongfully mark an area as a (section of a) spin domain. Repeated measurements solves this problem, but it could also be prevented, at least to a degree, by optimization of the FORT alignment and power. We have not yet performed such an optimisation.

Even better would be to use a higher power infrared laser than our present 5W laser, increasing the possible trap size. Currently, our atomic samples are only 10 pixels wide (in situ, in the radial direction) and it is therefore difficult to analyze the spin domains using image processing and to detect any fine detail in the spatial structure of the condensate mixture. Spin dependent images taken from a narrow condensate are also more sensitive to FORT vibrations. Creating a wider trap, by decreasing the sharpness of the focus, would result in (too) low densities inside the FORT at constant optical power of the used IR laser beam. By using a higher power laser, we could create a wide trap while at the same time have high densities to perform measurements. A higher power IR laser might also be used to create a wider range of trapping potential shapes.

5.4 CONCLUSION AND OUTLOOK

In this section, we have shown that the non destructive spatial imaging of a BEC of sodium atoms is possible using σ_+ and σ_- polarized light. First sodium atoms are trapped and cooled in a FORT and, using an RF sweep, spin polarized into BEC domains

of spin -1 and spin 0 particles relative to the \hat{z} axis. By rotating the quantization axis to lie along the probing direction, the \hat{y} axis, we are able to spatially image individual spin domains at a rate of 33.33 fps using two images taken 15ms apart using respectively σ_+ and σ_- light. Furthermore, we have shown that we are able to use our spin dependent PCI imaging technique to perform a measurement the spin drag coefficient between spin domains in a Bose-Einstein condensate.

Several improvements can be made to both our technique and experiment, for instance a higher imaging repetition rate, a stronger magnetic field into the \hat{y} direction, or an offset lock to ensure low phase accumulation. Other improvements could be made by creating a Bose-Einstein condensate that is spin polarized into equal parts of spin 0 and spin -1, and the experimental verification of the scaling parameters a and b to get absolute densities.

Bibliography

- [1] Arndt, R., "Analytical Line Shapes for Lorentzian Signals Broadened by Modulation" *Journal of Applied Physics*, 36-8, p2522-2525 August 1965.
- [2] Silver, J. A., "Frequency-modulation spectroscopy for trace species detection: theory and comparison among experimental methods", *Applied Optics*, 31-6, p707-717, February 1992.
- [3] Preston, D. W., "Doppler-free saturated absorption: Laser spectroscopy", *American Journal of Physics*, 64, p1432-1436, 1996
- [4] Kopka, H., Daly P.W., *A Guide to LaTeX*, Addison-Wesley, Reading, MA, 1999.
- [5] 't Woud, M. "Spin drag below the condensation temperature of an ultra-cold Bose gas", *Masters Thesis*, University of Utrecht, 2013.
- [6] Smits, J. "Formation of Faraday patterns in cigar-shaped Bose-Einstein condensates", *Masters Thesis*, University of Utrecht, 2013.
- [7] Metcalf, H. J., van der Straten, P., *Laser Cooling and Trapping*, Springer, New, NY, 1999.
- [8] Meppelink, R., "Hydrodynamic Excitations in a Bose-Einstein condensate", Ph.D. Thesis, University of Utrecht, Utrecht, 2009
- [9] Koller, S., "Experiments on Hydrodynamic Transport in Ultra-Cold Bose Gases", Ph.D. Thesis, University of Utrecht, Utrecht, 2012
- [10] "Saturated Absorption Spectroscopy", www.phys.ufl.edu/courses/phy4803L/group_III/sat_absorbtion/satabs.pdf, University of Florida
- [11] Shu-Wei Song, Lin Wen, Chao-Fei Liu, S.-C. Gou, and Wu-Ming Liu, "Ground states, solitons and spin textures in spin-1 bose-einstein condensates", *Frontiers of Physics*, 8(3):302-318, 2013.
- [12] Daniel A. Steck. Sodium D line data. <http://steck.us/alkalidata>, (revision 2.0.1, 2 May 2008)
- [13] Hecht, E. (2001). *Optics* (4th ed.). p. 378. ISBN 0805385665

Part IV

APPENDIX

The Lock-in Technique

We want to lock our laser to the top of an atomic absorption profile of a single atomic hyperfine transition by using a feedback loop to control the laser diode current. To identify the top of our absorption profile, a signal that is proportional to its first derivative is needed. It is easy to show that we can achieve this by modulating the laser frequency with a frequency ω_m .

Define the dimensionless laser frequency $\tilde{\omega} = \omega/\omega_{1/2}$ and $\tilde{\omega}_m = \omega_m/\omega_{1/2}$, where $\omega_{1/2}$ is the natural linewidth of the transition and ω and ω_m are the laser and modulation frequency respectively. Suppose we modulate the laser frequency in the following way:

$$\tilde{\omega}(t) = \tilde{\omega}_{center} + m \cos(\omega_m t) \quad (42)$$

The modulation index m represents the depth of the frequency modulation in terms of $\omega_{1/2}$. Suppose light is absorbed by some atomic spectral feature defined by the an atomic absorption line-shape function $G(x)$. Then the signal detected at some detector is given by:

$$S(\tilde{\omega}) = G[\tilde{\omega} + m \cos(\omega_m t)] \quad (43)$$

Defining the Fourier transform of G as $g(y) = \mathcal{F}(G(x))$,

$$s(y) = g(y) \exp(imy \cos(\omega_m t)) \quad (44)$$

Which can be expanded into the following Fourier series using the Jacobi-Anger formula to:

$$s(y) = \sum_{n=0}^{\infty} i^n \epsilon_n \cos(n\Omega t) g(y) J_n(my) \quad (45)$$

with $\epsilon_0 = 1$ and $\epsilon_n = 2$ for all $n \in \mathbb{N}^+$.

Setting $G(x) = \frac{1}{1+x^2}$, a standard Lorentzian line-shape, $g(y)$ becomes $g(y) = \frac{1}{2} \exp(-|y|)$. The derivative of $G(x)$ is $G'(x) = \frac{-2x}{1+x^2}$. By using the inverse Fourier transform,

$$S(x) = \frac{1}{2} \sum_{n=0}^{\infty} i^n \epsilon_n \cos(n\Omega t) \times \int_{-\infty}^{\infty} \exp(-|y|) \exp(ixy) J_n(my) dy \quad (46)$$

After integrating, this can be simplified to

$$S_n(x) = \frac{1}{2} \frac{1}{m^n} \epsilon_n i^n \left[\frac{(((1-ix)^2 + m^2)^{1/2} - (1-ix))^n}{((1-ix)^2 + m^2)^{1/2}} + c.c. \right] \quad (47)$$

$$S(x) = \sum_{n=0}^{\infty} i^n S_n(x) \cos(n\Omega t) \quad (48)$$

By using a lock-in amplifier to modulate the laser frequency and demodulate the measured intensity signal, the S_1 can be extracted. The Lock-in amplifier multiplies the measured signal by $\cos(\omega_m t + \phi)$ using an internal mixer. By adjusting the phase ϕ and by integrating the resulting signal using an integrator, the oscillating part the S_1 part

of 48, can be eliminated. After elimination of the imaginary parts and a expansion in powers of m , S_1 looks like:

$$S_1(x) = \frac{-2xm}{(1+x^2)^2} + O(m^3) \sim G'(x) \quad (49)$$

which for small m is directly proportional with the derivative of the line-shape function $G(x)$. For small frequency deviations from the absorption peak, we now have a linearly proportional signal that can be used by a PID controller to stabilize the laser frequency by adjusting the laser current and grating angle.

Polarization States and Transition Strength

We wish to calculate the transition strength of the sodium-23 D2 transition $|F_g = 1, m_g = 1\rangle \rightarrow |F_e = 1, m_e\rangle$ as a function of the polarization state of light after having passed a $\lambda/4$ or $\lambda/2$ waveplate in the case where a magnetic field is pointing into the \hat{z} or \hat{y} direction. To this end, we make use of the convenient notation of Jones calculus, albeit in a slightly altered way to accommodate our needs. The book Optics by Hecht has a nice explanation about Jones calculus in general [13]. Let \hat{y} be the propagation direction for our light and \hat{z} and \hat{x} be our base vector for defining the polarization state. Let the direction of the initial linear polarization state be defined as:

$$\vec{P}_{in} = 1\hat{x} + 0\hat{y} + 0\hat{z} = \begin{bmatrix} 1 \\ 0 \\ 0 \end{bmatrix} \quad (50)$$

Note that is actually impossible for light to have any polarization component in its direction of propagation, but leaving in the \hat{y} component of the polarization vector will enable us to use some convenient notation later on.

We can respectively represent a quarter and half wave plate with its fast axis in the \hat{x} direction and its surface normal into the \hat{y} direction as

$$A_{\lambda/2} = \begin{bmatrix} -1 & 0 & 0 \\ 0 & 0 & 0 \\ 0 & 0 & 1 \end{bmatrix} \quad (51)$$

$$A_{\lambda/4} = \begin{bmatrix} 1 & 0 & 0 \\ 0 & 0 & 0 \\ 0 & 0 & i \end{bmatrix} \quad (52)$$

Using the rotation matrix for rotations around the \hat{y} axis

$$R(\theta) = \begin{bmatrix} \cos(\theta) & 0 & -\sin(\theta) \\ 0 & 1 & 0 \\ \sin(\theta) & 0 & \cos(\theta) \end{bmatrix} \quad (53)$$

The polarization state of light after having passed a wave plate rotated over an angle θ then becomes

$$\begin{aligned} \vec{P}_{\lambda/2} &= R(\theta)A_{\lambda/2}R(-\theta)\vec{P}_{in} = \cos(2\theta)\hat{x} + \sin(2\theta)\hat{z} \\ \vec{P}_{\lambda/4} &= R(\theta)A_{\lambda/4}R(-\theta)\vec{P}_{in} \\ &= (\cos(\theta)^2 + i\sin(\theta)^2)\hat{x} + (1 - i)\cos(\theta)\sin(\theta)\hat{z} \end{aligned} \quad (54)$$

To get the appropriate transition strength using the transition strengths for pure σ_{\pm} and π polarized light as a function of the polarization state, the polarization needs to be

represented in terms of σ_+ , σ_- and π polarization. For the two imaging situations at hand, either \vec{H} is directed along the \hat{z} or \hat{y} axis and these cases will therefore be treated separately.

When the \vec{H} field is directed along the \hat{z} direction, any polarisation component in the \hat{z} direction is by definition π polarized light. To find the σ polarized components, we make use of the definition of left and right handed circular polarized light traveling into the \hat{z} direction to define a new basis in which to express the polarization state of the light:

$$\begin{aligned}\hat{\sigma}_- &= \frac{1}{\sqrt{2}}(\hat{x} + i\hat{y}) \\ \hat{\sigma}_+ &= \frac{1}{\sqrt{2}}(\hat{x} - i\hat{y}) \\ \hat{\pi} &= \hat{z}\end{aligned}\tag{55}$$

It then follows that the polarization state of

$$\begin{aligned}\hat{x} &= \frac{1}{2}(\hat{x} - i\hat{y}) + \frac{1}{2}(\hat{x} + i\hat{y}) = \frac{1}{\sqrt{2}}\hat{\sigma}_+ + \frac{1}{\sqrt{2}}\hat{\sigma}_- \\ \hat{z} &= \hat{\pi}\end{aligned}\tag{56}$$

Where the \hat{y} component is omitted because it is not needed, i.e. any component along it should be zero.

For the case where the \vec{H} field is pointing into the \hat{y} direction, we need circular polarized light traveling into the \hat{y} direction. Substituting \hat{y} for \hat{z} in equation 55 it follows that in this case

$$\begin{aligned}\hat{\sigma}_- &= \frac{1}{\sqrt{2}}(\hat{x} + i\hat{z}) \\ \hat{\sigma}_+ &= \frac{1}{\sqrt{2}}(\hat{x} - i\hat{z}) \\ \hat{\pi} &= 0\end{aligned}\tag{57}$$

In this case, there can be no $\hat{\pi}$ polarized light due to the propagation direction of the light. It follows that now the polarization components of the light are expressed as:

$$\begin{aligned}\hat{x} &= \frac{1}{2}(\hat{x} - i\hat{z}) + \frac{1}{2}(\hat{x} + i\hat{z}) = \frac{1}{\sqrt{2}}\hat{\sigma}_+ + \frac{1}{\sqrt{2}}\hat{\sigma}_- \\ \hat{z} &= \frac{i}{2}(\hat{x} - i\hat{z}) - \frac{i}{2}(\hat{x} + i\hat{z}) = \frac{i}{\sqrt{2}}\hat{\sigma}_+ - \frac{i}{\sqrt{2}}\hat{\sigma}_-\end{aligned}\tag{58}$$

To find the total transition strength, we now only need find the weighted contribution of the σ_+ , σ_- or π of the polarizations by multiplying each component with its appropriate transition strength \mathcal{S} from figure 14:

$$\mathcal{D} = \left(\vec{P} \cdot \vec{P}_{\sigma_+}\right) \mathcal{S}_{\sigma_+} + \left(\vec{P} \cdot \vec{P}_{\sigma_-}\right) \mathcal{S}_{\sigma_-} + \left(\vec{P} \cdot \vec{P}_{\pi}\right) \mathcal{S}_{\pi}\tag{59}$$

For specifically the $F_g = 1, m_g = -1 \rightarrow F_e = 1, m_e$ transition, we see from 14 that the transitions strength for σ_+ , σ_- and π polarizations respectively are $\frac{25}{60}$, 0, and $\frac{25}{60}$ ¹.

¹ Of course, here $\vec{a} \cdot \vec{b} = \vec{a} \vec{b}^\dagger$ where \vec{b}^\dagger is the complex conjugate of \vec{b}

Using the above definitions, the polarization states can be written as follows. When the \vec{H} field is directed along the \hat{z} direction:

$$\begin{aligned}\vec{P}_{\lambda/2}^{H_z} &= \cos(2\theta)\hat{x} + \sin(2\theta)\hat{z} \\ &= \frac{1}{\sqrt{2}}\cos(2\theta)\hat{\sigma}_+ + \frac{1}{\sqrt{2}}\cos(2\theta)\hat{\sigma}_- + \sin(2\theta)\hat{\pi}\end{aligned}\quad (60)$$

$$\begin{aligned}\vec{P}_{\lambda/4}^{H_z} &= (\cos(\theta)^2 + i\sin(\theta)^2)\hat{x} + (1-i)\cos(\theta)\sin(\theta)\hat{z} \\ &= \frac{1}{\sqrt{2}}(\cos(\theta)^2 + i\sin(\theta)^2)\hat{\sigma}_+ \\ &\quad + \frac{1}{\sqrt{2}}(\cos(\theta)^2 + i\sin(\theta)^2)\hat{\sigma}_- \\ &\quad + (1-i)\cos(\theta)\sin(\theta)\hat{\pi}\end{aligned}\quad (61)$$

Using equation 59 the transition strengths for the half and quarter wave plate case when the magnetic field is directed along the \hat{z} axis is therefore:

$$\mathcal{D}_{\lambda/2}^{H_z} = \frac{5}{48}(3 - \cos(4\theta)) \quad (62)$$

$$\mathcal{D}_{\lambda/4}^{H_z} = \frac{5}{96}(5 - \cos(4\theta)) \quad (63)$$

Applying the same procedure to the case that \vec{H} is in the \hat{y} direction:

$$\begin{aligned}\hat{P}_{\lambda/2}^{H_y} &= \cos(2\theta)\hat{x} + \sin(2\theta)\hat{z} \\ &= \cos(2\theta)\left(\frac{1}{\sqrt{2}}\hat{\sigma}_+ + \frac{1}{\sqrt{2}}\hat{\sigma}_-\right) + \sin(2\theta)\left(\frac{i}{\sqrt{2}}\hat{\sigma}_+ - \frac{i}{\sqrt{2}}\hat{\sigma}_-\right) \\ &= \frac{1}{\sqrt{2}}(\cos(2\theta) + i\sin(2\theta))\hat{\sigma}_+ + \frac{1}{\sqrt{2}}(\cos(2\theta) - i\sin(2\theta))\hat{\sigma}_-\end{aligned}\quad (64)$$

$$\begin{aligned}\hat{P}_{\lambda/4}^{H_y} &= (\cos(\theta)^2 + i\sin(\theta)^2)\hat{x} + (1-i)\cos(\theta)\sin(\theta)\hat{z} \\ &= (\cos(\theta)^2 + i\sin(\theta)^2)\left(\frac{1}{\sqrt{2}}\hat{\sigma}_+ + \frac{1}{\sqrt{2}}\hat{\sigma}_-\right) + \\ &\quad (1-i)\cos(\theta)\sin(\theta)\left(\frac{i}{\sqrt{2}}\hat{\sigma}_+ - \frac{i}{\sqrt{2}}\hat{\sigma}_-\right) \\ &= \frac{1}{\sqrt{2}}((\cos(\theta)^2 + i\sin(\theta)^2) + i(1-i)\cos(\theta)\sin(\theta))\hat{\sigma}_+ + \\ &\quad \frac{1}{\sqrt{2}}((\cos(\theta)^2 + i\sin(\theta)^2) - i(1-i)\cos(\theta)\sin(\theta))\hat{\sigma}_-\end{aligned}\quad (65)$$

Again taking the weighted polarization, the transition strengths are:

$$\mathcal{D}_{\lambda/2}^{H_y} = \frac{5}{24} \quad (66)$$

$$\mathcal{D}_{\lambda/4}^{H_y} = \frac{5}{24}(1 + \sin(2\theta)) \quad (67)$$

In the special application of spin PCI, we use the difference in transition strength for different light polarization to distinguish different spin types from one another. We see

that in the case that the magnetic field is orientated in the H_z direction, the transition strength for the $F_g = 1, m_g = 1 \rightarrow F_e = 1, m_e$ transition goes from $\frac{5}{12}$ to $\frac{5}{24}$, while in the case that the magnetic field is orientated in the H_y direction, the transition strength varies from 0 to $\frac{25}{60}$. If we want to maximize the contrast using Spin PCI, rotating the magnetic field gives us a 2 times stronger contrast. Figure 29 graphically shows the difference in contrast for the different polarization states.

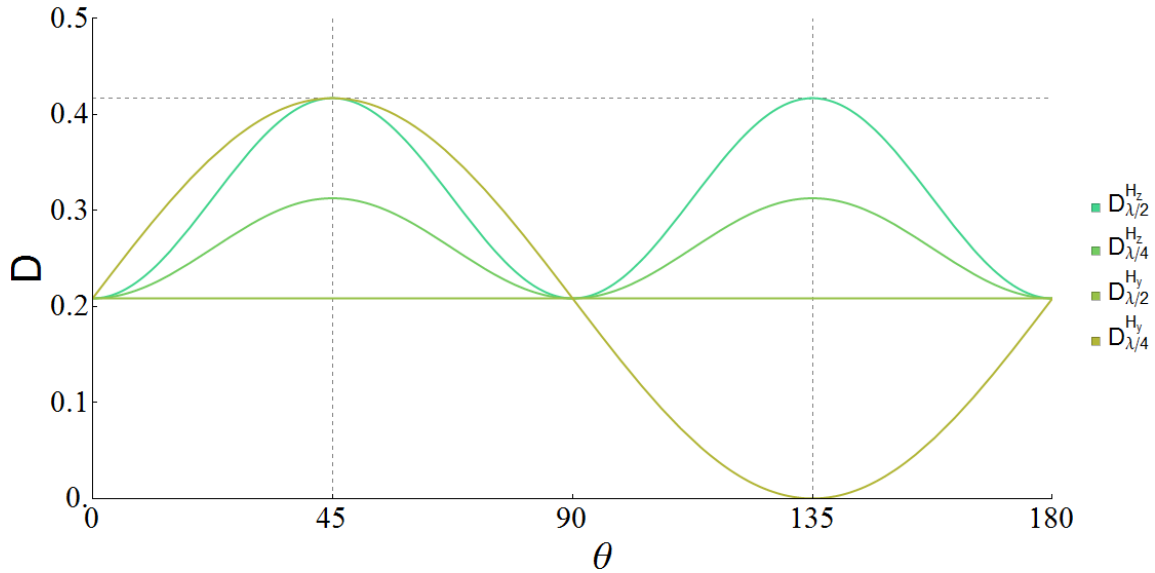


Figure 28.: Calculated transition strength as a function of the polarization state created sending linearly polarized light through a rotated quarter and half wave plate with the magnetic quantization axis orientated into respectively the \hat{z} and \hat{y} direction when probing into the \hat{y} direction. Note that using a magnetic field aligned parallel to the \hat{y} axis, a twice as high contrast is achievable when using different polarizations to image a state.

Cable Connections of the TA-SHG Pro



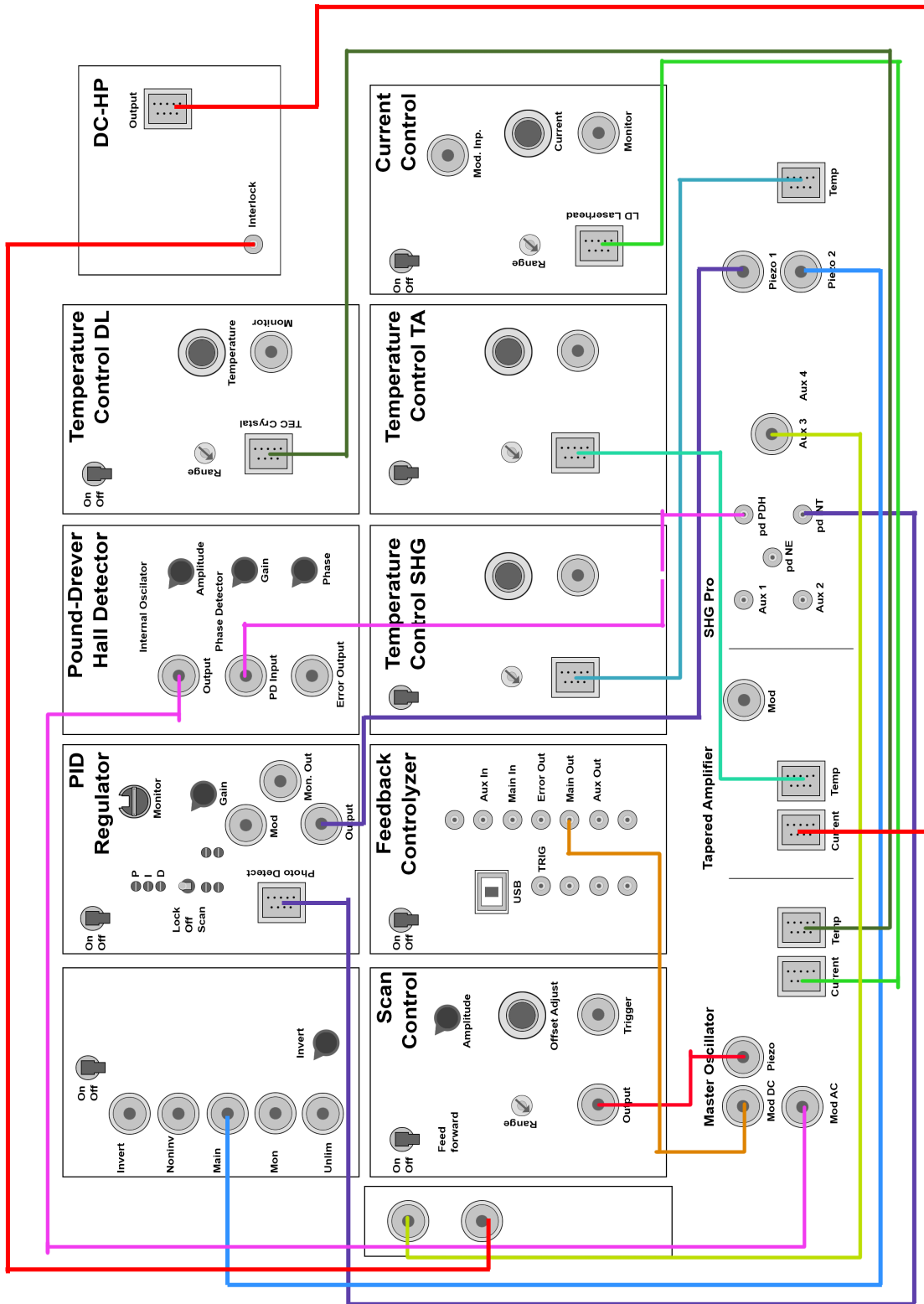


Figure 29.: Cable connections in a standard setup of the TA-SHG Pro

Imaging Script Examples

Writing a Python scripts to imaging the created spin dependent PCI images is quite straightforward, but to give a starting point here some small examples are listed anyone can use to improve on. I have to thank Pieter Bons for helping me along, I modified some small snippets he had.

Fourier Filter

A program that eliminates all frequency components 8 orders of magnitude below that highest peak in the FFT spectrum of an image. Used for noise reduction. Can easily be modified to block out unwanted frequency components from the FFT spectrum by using masks.

```
import pyfits
import pylab
import scipy.odr
from numpy import *
import numpy as np
import datetime
from array import *
from StringIO import StringIO

def filter(img):
    imghigh = np.greater(img, 0)
    imglow = np.less(img, 10)

    fimg1 = np.fft.fft2(img*imghigh*imglow)
    fimgs1 = np.fft.fftshift(fimg1)
    fimgpowers1 = np.log10(np.abs(fimgs1)**2)

    mask = np.ones((img.shape))

    # Cutoff of noise in the fft
    maxvalfft = np.max(fimgpowers1)
    fimgpowers2 = fimgpowers1 - maxvalfft
    highpassfilter=np.greater(fimgpowers2,-8)

    # Mask to cut away blocks of unwanted interference from the fft spectrum
    # mask[57:71,388:408]=0
    # mask[70:84,599:620]=0

    fftfilter = fimgs1*highpassfilter*mask
```

```

bimg = np.fft.ifftshift(fftfilter)
bimg = np.fft.ifft2(bimg)
bimg = np.abs(bimg)

return bimg

```

Spin Dependent Image Viewer

Simple routine to view a single reconstructed image from a spin dependent PCI image series. An image file is loaded from a folder, and stored in an array. The array has dimensions (number of images) \times (height) \times (width). The variable 'nr' identifies the image file number, and 'plnr' identifies the image number inside a single imaging series. By choosing constants a and b a superposition of image a and b is created. Needs the filter function from above, and pyfits/pylab.

```

def viewab(nr, plnr, a, b):
    # Path
    date='20140702'
    filename=(date+nr)
    path=('/home/projects/strdata/bec/'+date+'/')

    #Import Image File
    hdulista = pyfits.open(path+filename+'0.fit')
    hdulistb = pyfits.open(path+filename+'1.fit')
    hdulisc = pyfits.open(path+filename+'2.fit')
    imgsraw=hdulista[0].data
    imgsback=hdulistb[0].data
    imgsdark=hdulisc[0].data
    imgssingle=(imgsraw-1*imgsdark)/(imgsback-1*imgsdark+0.000001)

    # create an array of all PCI images; shape[0]/2 is the total number of a
    # I1 - b I2 images
    imgarray = np.zeros((imgssingle.shape[0]/2,imgssingle.shape[1],imgssingle.
        shape[2]))

    # Apply a fourier filter and create the superposition of images
    for i in range(0,imgarray.shape[0]):
        imgarray[i,0:imgssingle.shape[1],0:imgssingle.shape[2]] = (a*filter(
            imgssingle[2*i+1,:,:]) - b*filter(imgssingle[2*i,:,:])+(b-a))

    plt.imshow(imgarray[plnr,:,:],vmin = -3.0, vmax = 3.0, aspect='auto',cmap=
        'bwr')
    pylab.colorbar()
    plt.show()

```

SVD Saving Routine

A routine that will save all image data to CSV files to be handled by other programs. I used Mathematica to prepare images and to easily assign CMYK colors to numerical values and create a function that blends colors, but everything could be done in Python as well. Mathematica was chosen to dynamically change parameters, like from which pixels to cut the PCI image or how many pixels wide the rolling median filter should be.

The function CMYK assigns a vector of CMYK values to a numerical value. These vectors can be added to naturally produce blends of colors when rendered as a CMYK value.

```
def svddatasave(nr, plnr):
    # Path
    date='20140702'
    filename=(date+nr)
    path=('/home/projects/strdata/bec/christian/fit/')

    #Import SVD picture
    hdulista = pyfits.open(path+filename+'_svd.fit')
    imgssingle=hdulista[0].data

    #Scale parameters
    amin = -1.753
    bmin = -1.653
    anul = -1.46
    bnul = -2.166

    x1 = 0
    x2 = 900
    y1 = 50
    y2 = 110

    sizex = x2 - x1
    sizey = y2 - y1

    # create an array of all PCI images; shape[0]/2 is the total number of a
    # I1 - b I2 images
    imgarraymin = np.zeros((imgssingle.shape[0]/2,sizey,sizex))
    imgarraynul = np.zeros((imgssingle.shape[0]/2,sizey,sizex))

    # Apply a fourier filter and create the superposition of images
    for i in range(0,imgarraymin.shape[0]):
        imgarraymin[i,0:sizey,0:sizex] = (amin*filter(imgssingle[2*i+1,y1:y2,x1:
            x2]) - bmin*filter(imgssingle[2*i,y1:y2,x1:x2]))+(bmin-amin)
        imgarraynul[i,0:sizey,0:sizex] = (anul*filter(imgssingle[2*i+1,y1:y2,x1:
            x2]) - bnul*filter(imgssingle[2*i,y1:y2,x1:x2]))+(bnul-anul)

    # Output files for saving
    outputfilemin = open(str(nr)+"_"+str(plnr)+"_-1".txt", "w")
    outputfilenul = open(str(nr)+"_"+str(plnr)+"_0".txt", "w")
```

```

for i in range(0, imgarraymin.shape[1]):
    for j in range(0, imgarraymin.shape[2]):
        outputfilemin.write(str(imgarraymin[plnr,i,j])+",")
        outputfilenul.write(str(imgarraynul[plnr,i,j])+",")
    outputfilemin.write("\n")
    outputfilenul.write("\n")
outputfilemin.close()
outputfilenul.close()

```

Mathematica code to export cut out images of both spin -1 and spin 0 particles, based on assigning a color value to a numerical pixel value. Values above/below the max threshold become clipped.

```

(*Maximum value for the images. Pixel values higher/lower that this will
   become clipped*)
maxval = 4;

(*Function to assign a CMYK color to a numerical value*)
cmyk[x_] :=
If[x < 0, {Min[-x/maxval, 1], Min[-x/maxval, 1], 0, 0}, {0, Min[x/maxval,
1],
Min[x/maxval, 1], 0}]

(*Number of images in a series*)
nn = 10

(*Files need to be in the same directory, or a path should given*)
filenames =
Transpose /@
Transpose[
Partition[#, nn] & /@ Transpose[Partition[FileNames["*.txt"], 2]]];

(*Pixel values to cut out from the imported image files*)
y0 = 7;
y1 = 23

For[i = 1, i <= Length[filenames], i++,
For[j = 1, j <= nn, j++,
minimg =
Map[cmyk, (Most /@ Import[filenames[[i, j, 2]], "CSV"])[[u0 ;; u1,
All]], {2}];
nuling =
Map[cmyk, (Most /@ Import[filenames[[i, j, 1]], "CSV"])[[u0 ;; u1,
All]], {2}];
Export[
"C:\\Users\\Chris\\Desktop\\Masterscriptie\\Betere_Spin\\PCI\\pictures\\"
<> StringTake[filenames[[i, j, 1]], 6] <> ".png",
Image[nuling + minimg, ColorSpace -> "CMYK", ImageSize -> 900]]
]
]

```

Acknowledgements

No master thesis would be complete without the semi-obligatory round of acknowledgements, I suppose.

Obviously starting with people on top of the food chain: **Peter**. None of this would have been possible without the guidance and supervision provided by you, for which I express my gratitude. Your enthusiasm for and confidence in your students is quite catchy. The days you helped me in the lab were not only helpful, but also fun. To **Pieter**, thank you for your patience and support. Without it surely I would have lost my mind a long time ago. I would also like to use this opportunity to thank a very special person, known to most of us by her MPC designation, 1 Ceres. Maybe next time she orbits around, you can radio her my gratitude, Pieter. I would also need to thank **Alexander** for all help with dealing with the initial troubles with the TA-SHG laser system. Setting things on fire and the occasional misuse of liquid nitrogen was also pretty cool, haha. And I think I should thank **Dries** for at least not stealing and/or eating all winegums and liquorice from our lab. Most memorable lab moment is also credited to you, when you stated (while watching over the pressure gauges after the vacuum failure incident) that you were, in fact, a "(...) with an attitude" in reference to the 2005 Snoop Dogg hit classic "Drop it like it's Hot". **Ole, Sandy, Arjon** and **Sebastiaan** have my thanks in helping me with all kinds of various stuff, from lighters, to parts and ideas, to some help with Python and (in Arjon's case) dropping by Thursday afternoon with a good idea. **Frits** and **Dante**, you have helped me so many times, I have no idea how I could ever return the favor. All the stories about Dries and Peter were also incredibly amusing, haha. **Cees**, you helped me a lot in thinking over the experimental setup and ensuring everything was sufficiently thought through, and fixing all kinds of stuff. From collimators to the Wavemeter. If I had to do it myself, I would still be stuck in the lab. To **Paul**, the man who can fix it all, no matter if I'd want some metal caps, a hacksaw or an O-ring you'd always deliver. Good luck with battling that cycling bridge.

Johan, thanks for all the help during the first half year. I also enjoyed the virus model afternoon. I haven't tried it on Ebola yet, but maybe I'll try it out once I'm done. **Martijn**, I'm trying as hard as I can to come up with something witty about trains... but it's not working. Much like the train system itself each and every time I use is. **Stefan**, non-linear youtube cat dynamics is all I can say. **Jasper**, always the guy with a good idea. **Damaz**, global domination will be ours eventually. I'm sure of it. Once Lockinvest takes to the skies I'll give you a call. **Thijs, Maxim, and Rens**, you guys were quite funny. I'm kind of beginning to run out of compliments here, but know I enjoyed working with you.

Now, there are many other people I could thank for being there the past 1.5 years. But, instead of writing all of you up in the acknowledgement section of this thesis, I'll thank each of you in person.